JMEPEG (2024) 33:6146–6163
https://doi.org/10.1007/s11665-023-08353-y

1059-9495/$19.00

TECHNICAL ARTICLE

Microstructure and Tensile Property of Al_3Zr/Al-Cu-Ni-V Composite Prepared by In Situ Reaction

Junge Cui, Guangkai Zeng, Nikhil Gupta, Yue Luo, Xiangzhou Fu, Hailong Yang, Anmin Li, and Liwen Pan

Submitted: 8 December 2022 / Revised: 12 April 2023 / Accepted: 16 May 2023 / Published online: 31 May 2023

In this work, the high-temperature stable $D0_{23}$-Al_3Zr was introduced to an Al-Cu-Ni-V alloy to improve the HT (350 °C) mechanical properties by the melt in situ reaction. The effect of Al_3Zr contents and T6 heat treatment on the microstructure, room temperature, and high-temperature tensile properties of the Al_3Zr/Al-6Cu-2Ni-0.5 V composites was investigated. The α-Al, Al_2Cu, Al_3Ni, Al_3CuNi, Al_7Cu_4Ni, and Al_3Zr phases were present in the as-cast composites. The amount of the fine (2-4 μm) blocky $D0_{23}$-Al_3Zr increases with the increased addition of K_2ZrF_6 salt. After T6 heat treatment, the dispersed fine θ′-Al_2Cu precipitates (200-300 nm) formed in the matrix. The interconnected structure of the Al_3CuNi phase was broken, became spherical and coarsened. In addition, the Al_3Zr particles had higher Cu content and changed from blocky to elliptical or spherical shapes without changing the tetragonal crystal structure after the T6 treatment. The highest HT tensile strength was observed for the as-cast composite containing 12 wt.%Al_3Zr, reaching 118 MPa, 35.48% higher than the base alloy. After the T6 treatment, the tensile strength of 9 wt.%Al_3Zr/Al-6Cu-2Ni-0.5 V composite at room and the elevated temperature reached 288.5 and 143.1 MPa, respectively. The analysis shows that the addition of K_2ZrF_6 not only introduced the high thermal stability $D0_{23}$-Al_3Zr, but also promoted the precipitation and refinement of the θ′-Al_2Cu after aging. The improvement of high-temperature mechanical properties of the composites is mainly attributed to the precipitation strengthening of the $D0_{23}$-Al_3Zr phase and the dispersion strengthening by the θ′-Al_2Cu phase that indirectly modifies by K_2ZrF_6.

Keywords Al-Cu-Ni-V alloy, heat treatment, high-temperature property, microstructure

1. Introduction

Heat-resistant Al-alloys have low density and high specific strength, creep resistance, and oxidation resistance and are widely used in automobiles, aerospace, and marine vessels for applications such as pistons, cylinder liners, connecting rods, and cylinder heads (Ref 1-3). The traditional cast Al-Si and Al-Cu alloys are used up to 300 °C; e.g., A356 and 319 alloys are used up to 250 °C because the eutectic Si, Al_2Cu, Mg_2Si, and Al_2CuMg phases coarsen or dissolve above 200 °C, leading to a loss of their strengthening effect (Ref 4, 5). The new high-performance engines operating above 300 °C require alloys that can provide high-temperature (HT) strength (Ref 6), such as pistons, cylinder liners, and cylinder heads of diesel engines in high-power vehicles and tanks. Introducing a high thermal stability strengthening phase into the Al-alloy can help develop alloys with higher service temperatures and replace the expensive Ti alloy or the heavy steels in some applications (Ref 7).

Transition metals or rare earth elements (Er, Hf, Ti, Zr, Nb, V, Y, Sc and Ni) have been added to Al-alloys to form a stable or metastable $L1_2$-Al_3M strengthening phase for improvement in HT temperature properties (Ref 8-23). Microalloying with Zr, Ti, and V has been studied to improve the HT properties of Al-alloys (Ref 8, 24). Results show that microalloying with Zr or Ti followed by aging can produce the high thermal stability phase $L1_2$-Al_3Zr or $L1_2$-Al_3Ti, respectively (Ref 25). V is usually added as a solute dissolving into Al_3Zr and Al_3Ti phases, which form thermally stable Al_3(Zr, V) and Al_3(Ti, V) phases (Ref 26-28) because Al_3(Zr, V) and Al_3(Ti, V) have a minor lattice mismatch with the Al matrix. Al_3Zr and its derivative phases (Al_3(Zr, V), Al_3(Zr, Sc), etc.) are considered strengthening phases with high thermal stability in the range of 300-500 °C. The introduction of Al_3Zr phases by microalloying and aging has made significant progress in the past two decades. Dinc Erdeniz et al. (Ref 29) reported that the $L1_2$-ordered, coherent Al_3(Er, Sc, Zr) nanoscale precipitates could strengthen the Al-Er-Sc-Zr-Si alloy for use up to 400 °C. After adding V into the Al-Er-Sc-Zr-Si alloy, the V-containing Al_3(Er, Sc, Zr, V) precipitates have a minor lattice parameter mismatch with the Al matrix, further improving the precipitates' thermal stability and coarsening resistance. Fan and Makhlouf showed (Ref 30) that the thermal stability of Al_3Zr and Al_3V is lower than $Al_3(Zr_x, V_{1-x})$ precipitates because the latter has a lower lattice mismatch with the Al matrix. In contrast, the thermal stabilities of the three are higher than that

Junge Cui, Guangkai Zeng, Yue Luo, Xiangzhou Fu, Hailong Yang, Anmin Li, and **Liwen Pan**, Guangxi Key Laboratory of Processing for Nonferrous Metals and Featured Materials, School of Resources, Environment and Materials, Guangxi University, Nanning 530004, China; and **Nikhil Gupta**, Composite Materials and Mechanics Laboratory, Department of Mechanical and Aerospace Engineering, Tandon School of Engineering, New York University, Brooklyn, NY 11201. Contact e-mail: panliwen@gxu.edu.cn.

of Al_3Sc because the thermal diffusivity of Zr and V in the Al matrix is much lower than Sc. Jinhua Ding et al. (Ref 31) investigated the effect of Mo, Zr, and Y on microstructure and high-temperature mechanical properties of Al-5.8Cu-0.3Mn-0.2 Mg alloy. The result shows that $L1_2$-Al_3(Zr, Y), Al_3Zr, Al_3Y, and $Al_{12}Mo$ precipitated after solution treatment. These precipitates were HT stable and could slow the coarsening rate of θ′-Al_2Cu precipitates. The high-temperature tensile strength was improved significantly due to the dispersion strengthening by $L1_2$-Al_3(Zr, Y), Al_3Zr, Al_3Y, $Al_{12}Mo$, and the modified θ′-Al_2Cu. Shaha et al. (Ref 28) studied the effect of the micro-addition of Ti, Zr, and V on the microstructure of Al-Si-Cu-Mg alloy. It was indicated that several $(AlSi)_x$(TiVZr) phases with $D0_{22}$/$D0_{23}$ tetragonal crystal structures and different lattice parameters formed. The $(AlSi)_x$(TiVZr) phases were stable up to 696-705 °C, helping to enhance the high-temperature properties. However, generally, the solid solubility of most transition metals or rare earth elements in the Al matrix is very low, leading to only a small volume fraction of uniformly dispersed precipitates even after a long aging time (Ref 32).

Apart from the effects of microalloying, the thermal stability of the traditional strengthening phases, such as the θ′-Al_2Cu strengthening phase in the Al-Cu alloy, has been widely studied. It is found that Sc, Ti, Mn, Zr, V, and Nb can promote the precipitation of θ′-Al_2Cu and slow down its growth and coarsening in the Al-Cu alloy (Ref 33-36). The results show that the nano-Al_3(Sc, Zr) core–shell dispersed phase precipitated first during artificial aging and acted as the nucleation site for θ′-Al_2Cu. The addition of Mn led to significant improvement in the hardness of the alloy after aging at 190 °C. Due to the improved dispersion and refinement of the θ′-Al_2Cu phase. It reduced its growth and coarsening rate at HT due to the segregation of Sc, Zr, and Mn at the coherent or semi-coherent interface of θ′-Al_2Cu.

The metastable $L1_2$-Al_3Zr phase strengthens Al-alloys by Zr microalloying and aging (Ref 37). However, using tetragonal $D0_{23}$-Al_3Zr to strengthen the Al-alloys for high-temperature applications is rarely reported. The equilibrium tetragonal structure of the $D0_{23}$-Al_3Zr phase is stable at higher temperatures than $L1_2$-Al_3Zr (Ref 38). The lattice parameters of Al_3Zr ($D0_{23}$) are $a = b = 0.4014$ and $c = 1.7321$ nm (Ref 32), and that of α-Al are $a = b = c = 0.40496$ nm. The lattice parameters a and b of these two phases closely match, while the c of Al_3Zr is almost four times that of α-Al (Ref 39). The morphology of $D0_{23}$-Al_3Zr prepared by the conventional alloying method is generally coarse and long, which is detrimental to the mechanical properties of the alloy. The melt in situ reaction can prepare the equiaxed, granular $D0_{23}$-Al_3Zr phase (Ref 15, 40); after adding K_2ZrF_6 salt to the aluminum melt, $13Al + 3K_2ZrF_6 \rightarrow 3Al_3Zr + 4AlF_3 + 6KF$ can occur with the aluminum melt, producing Al_3Zr phase (Ref 41). However, heat-resistant Al-alloys strengthened by the granular $D0_{23}$-Al_3Zr made by melt in situ reactions are scarcely reported, especially for HT mechanical properties.

Ni can also be used to improve the high-temperature mechanical properties of Al-alloys, mainly due to the formation of thermally stable phases ε-Al_3Ni, δ-Al_3CuNi, and γ-Al_7Cu_4Ni (Ref 42). The increased ε-Al_3Ni phase in Al-12Si-0.9Cu-0.8 Mg alloys benefited to the phase stability and tensile strength at 350 °C (Ref 17). The ultimate tensile strength increases from 94 MPa for 1.0% Ni to 116 MPa for 4.0% Ni. In another study, the tensile properties of Al-Cu-Mn-Fe-xNi (0.5 wt.%, 1.5 wt.%) alloy at 200 and 300 °C increased with the Ni content (Ref 43), which was attributed to thermally stable secondary intermetallic compounds Al_9FeNi and Al_3Cu-Ni.

The present work aims to introduce the HT stable strengthening phases of modified θ′-Al_2Cu, $D0_{23}$-Al_3(Zr, V) and Al_3Ni into the Al-alloy matrix to improve the high-temperature mechanical properties. The $D0_{23}$-Al_3Zr phase was introduced into Al-Cu-Ni-V alloy by melt in situ reaction. The effects of Al_3Zr content and heat treatment process on the microstructure and mechanical properties of Al-matrix composites at room temperature (RT) and HT (350 °C) were studied, which laid a foundation for developing new heat-resistant Al-alloy.

2. Experimental Procedure

2.1 Materials Used

The materials used in this work are pure Al (99.7 wt.%), K_2ZrF_6 (AR) salt, Al-50Cu, Al-10 V, and Al-10Ni master alloys to prepare the Al_3Zr/Al-6Cu-2Ni-0.5 V composites. Al_3Zr is incorporated in 3, 6, 9, and 12 wt.% quantities to synthesize four types of composites. The nominal and actual composition of the base and composites are shown in Table 1, and the weight of K_2ZrF_6 in the table is calculated according to the melt weight. The total weight of each melt is 550 g in this experiment. A melt coating agent (50% KCl + 50% NaCl, wt.%), a refining agent (C_2Cl_6), and a crucible coating (Sodium silicate/Zinc oxide = 1:3, wt.%) are also used.

2.2 Melting and Casting

A mid-frequency induction furnace (M.MF.00008 type) was used for smelting. First, the pure Al ingot was melted in the graphite crucible. Then, the melt coating agent was added to prevent burning loss. The melt temperature was controlled at 775 ± 5 °C for about 5 min, followed by slagging. The master alloys Al-10Ni, Al-10 V and Al-50Cu were added to the melt sequence. The covering agent has added again, and the melt temperature was held for 8 min, followed by slagging. Next, the melt was stirred at 600 rpm for 4 min using a graphite agitator, while the K_2ZrF_6 salt powder was continuously added. Finally, the smelt was held for 2-3 min after finishing stirring and slagged again when the melt cooled down to about 750 °C. After degassing, the melt was poured into a steel mold with a preheating temperature of 200 °C. The design and dimensions of the steel mold are shown in Fig. 1.

2.3 Heat Treatment and Heat Exposure

A Kington electric furnace (YYX1200-40 JINDUN) was used for the T6 heat treatment. The solutionizing time, solutionizing temperature, water quenching temperature, aging temperature, and aging time were maintained as 2 h, 550 °C, 25 °C, 175 °C and 8 h, respectively.

2.4 Sample Preparation

SEM sample preparation process: First, 10 × 10 × 10mm metallographic samples were cut from the casting; then, the samples were water-ground with 400 mesh, 800 mesh, 1200 mesh, and 2000 mesh sandpaper. Then, W2.5 water-soluble diamond polishing paste was used for polishing; the polished metallographic samples surface was wiped with absorbent

Table 1 Nominal composition and actual composition of the composites (wt.%)

	Alloy	K2ZrF6	Al	Cu	Zr	Ni	V	Si	Fe	Zn	Mo
Nominal composition	Base alloy	00.00	91.50	6.00	…	2.00	0.50	…	…	…	…
	3 wt.% Al3Zr composite	27.15	89.91	6.00	1.59	2.00	0.50	…	…	…	…
	6 wt.% Al3Zr composite	54.30	88.32	6.00	3.18	2.00	0.50	…	…	…	…
	9 wt.% Al3Zr composite	81.45	86.73	6.00	4.77	2.00	0.50	…	…	…	…
	12 wt.% Al3Zr composite	108.6	85.14	6.00	6.36	2.00	0.50	…		…	
Actual composition	Base alloy	…	90.66	5.79	…	2.03	0.47	0.80	0.135	0.122	…
	3 wt.% Al3Zr composite	…	89.66	5.97	1.42	1.97	0.52	0.09	0.103	0.228	0.019
	6 wt.% Al3Zr composite	…	87.80	6.05	2.92	2.06	0.45	0.21	0.091	0.380	0.036
	9 wt.% Al3Zr composite	…	86.63	5.77	3.80	1.95	0.46	0.81	0.119	0.430	0.043
	12 wt.% Al3Zr composite	…	84.43	5.98	4.45	2.01	0.47	0.39	0.210	0.299	0.043

cotton dampened with alcohol and dried it with a hair dryer. To observe the precipitation phase of the heat treatment samples by SEM, the operation method is as follows: Wash the polished sample with water or wipe off the remaining dirt on the surface with alcohol, and then immerse the abrasive surface of the polished sample into the caustic agent. The hydrofluoric acid was used to etch on the sample surface for 5-10 s, and then aqua regia was used to etch for 2-5 s. (The specific time depends on the corrosion degree of the sample.) The polished surface will gradually lose its luster; after the sample is corroded properly, rinse it with water immediately, blot it dry with filter paper or a hair dryer, and then observe it under a microscope. The depth of corrosion of the specimen depends on the material of the specimen, the structure of the specimen and the purpose of the microscopic analysis, and also depends on the magnification of the microscope required by the observer. The corrosion is slightly shallow at high magnification observation, while the corrosion should be deeper at low magnification observation.

TEM sample preparation: The wafers with a 3mm diameter and 2mm thickness were cut from the casting with an electric spark wire cutter, and the wafers were ground into 60-μm slices by hand. Then, the samples were thinned by dual-jet electrolytic polishing method at −30 °C in the electrolytic polishing solution (67% methanol + 33% nitric acid, volume fraction) at a voltage of 20 V, and the final thickness of the TEM samples reached 100-200 nm.

2.5 Microstructure Observation and Property Testing

The phase analysis was conducted by an x-ray diffractometer (XRD) (MiniFlex600 x-ray diffractometer) at the scanning speed of 6°/min. A Phenom ProX scanning electron microscope (SEM) equipped with an energy dispersive spectroscope (EDS) was used for microscopy and composition analysis. The crystal structures of phases were analyzed by selected area electron diffraction (SAED) using FETEM (JEM-2100F) at 200 kV. The RT and HT tensile tests were conducted on a WDW3100 computer-controlled electronic universal testing machine at a 0.5-mm/min crosshead displacement rate. The images and dimensions of the tensile specimens are shown in Fig. 2. For HT tests, the specimens were heated to 350 °C and homogenized for 20 min before loading.

3. Result

3.1 Microstructure Analysis

Figure 3 shows the microstructure of the synthesized composites containing different wt.% of Al_3Zr. The corresponding XRD patterns are shown in Fig. 3(f). The chemical composition of each detected phase, measured using EDS, is presented in Fig. 4. It is observed that the as-cast microstructure of the composites consists of α-Al, Al_2Cu, Al_3Ni, Al_7Cu_4Ni, Al_3CuNi, Al_3Zr, and $Al_{10}V$ phases. The Al-Al_2Cu eutectic regions having an elliptic morphology are sporadically scattered in the Al-matrix (spot 2 in Fig. 3). With the increase in K_2ZrF_6 quantity, the Al_3Zr also increases. In contrast, the Al-Al_2Cu eutectic decreases or even disappears. An increase in the dissolution of Cu in the Al_3Zr phase leads to a reduction in the Cu concentration in the Al-matrix, which decreases the Al-Al_2Cu eutectic. EDS analysis results in Fig. 4 (spot 6) show the

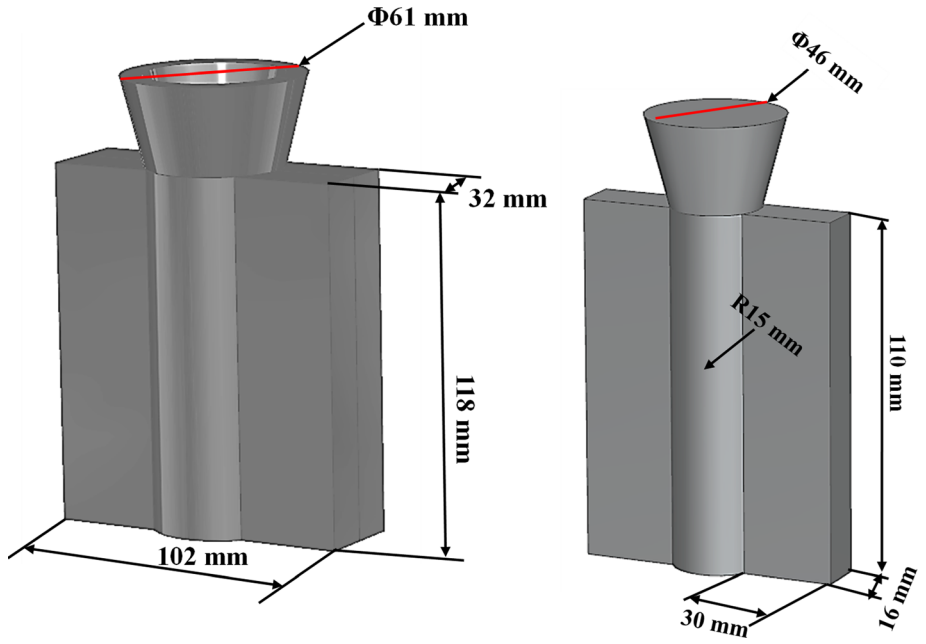

Fig. 1 Schematic diagrams of the steel mold and ingot casting: (a) steel mold (b) ingot casting

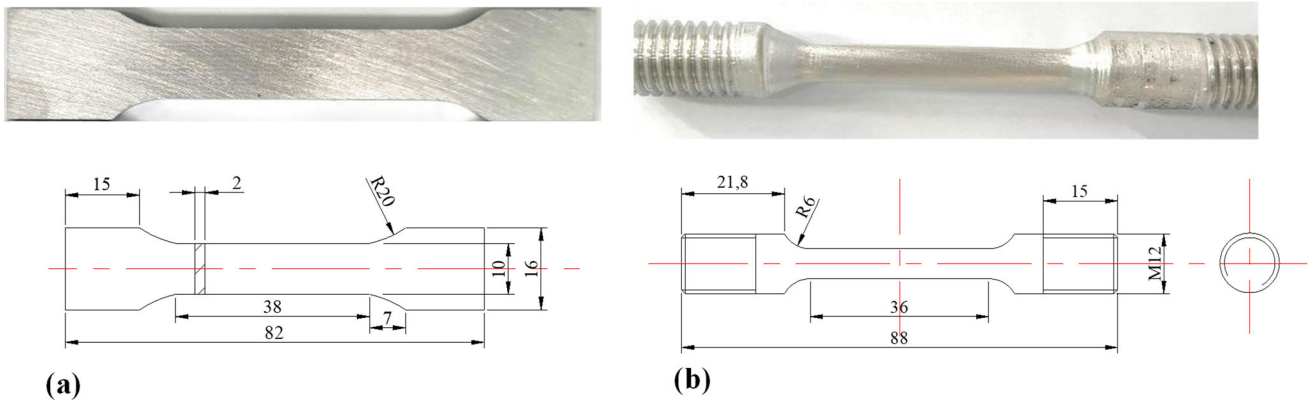

Fig. 2 Photographs and dimensions of the tensile specimens used for testing at: (a) room temperature and (b) 350 °C

presence of dissolved Cu in the Al_3Zr phase. The Al_3CuNi (spot 3) phase has the morphology of an interconnected network. The Al-Al_3CuNi eutectic decreases with the increase in Al_3Zr content, while Al_3Ni (spot 5) phase gradually increases because the dissolution of Cu in the Al_3Zr phase reduces its content in the matrix. The Al_7Cu_4Ni (spot 4) phase has the morphology of a short stick. Spot 6 is the blocky Al_3Zr phase with small amounts of dissolved Ni, V and Cu.

The size of the Al_3Zr phase is in the range of 2-4 μm. The Al_3Zr crystals with a tetragonal $D0_{23}$ structure are usually produced in the as-cast composite (Ref 44). The $D0_{23}$-Al_3Zr phase has higher thermal stability than $L1_2$-Al_3Zr (Ref 38). A small number of $Al_{10}V$ phase precipitates (spot 7) are also sporadically distributed in the matrix. TEM was used to clearly observe the morphology of the Al_3Zr phase in the 9 wt.%Al_3Zr composites. From the TEM photos (Fig. 5a), it can be seen that the morphology of Al_3Zr exhibits a nearly rectangular shape. The composition of Al_3Zr was analyzed using EDS in TEM (Fig. 5c), and it was found that the main element besides Al is Zr. Alat: (Zr + Cu + Ni + V) at is approximately 3:1. To further determine the structure of Al_3Zr, we used JADE6.5 to fit and calculate the Al_3Zr diffraction peaks in the XRD diffraction spectrum of the alloy, and the lattice constants of $D0_{23}$-Al_3Zr phase are $a = b = 4.012$ Å, $c = 17.331$ Å. The results indicate that the calculated lattice constant is consistent with the $D0_{23}$-Al_3Zr lattice constant data ($a = b = 4.014$ Å and $c = 17.321$ Å) obtained by Keith Knipling et al. (8, 32), thus determining that the Al_3Zr phase structure in this paper is $D0_{23}$. The SAD patterns of $D0_{23}$-Al_3Zr were calibrated based on lattice constants, as shown in Fig. 5(b).

3.2 Tensile Properties of as-Cast xAl_3Zr/Al-Cu-Ni-V Composites

The room- and high-temperature tensile stress–strain curves of the as-cast composites are shown in Fig. 6, and the calculated ultimate tensile strength (UTS), yield stress (σ_{YS}), fracture strain (ε_F) and elongation are compiled in Table 2. It is observed that the room temperature (RT) UTS of the base alloy and composites is unchanged (203-208 MPa) for Al_3Zr content

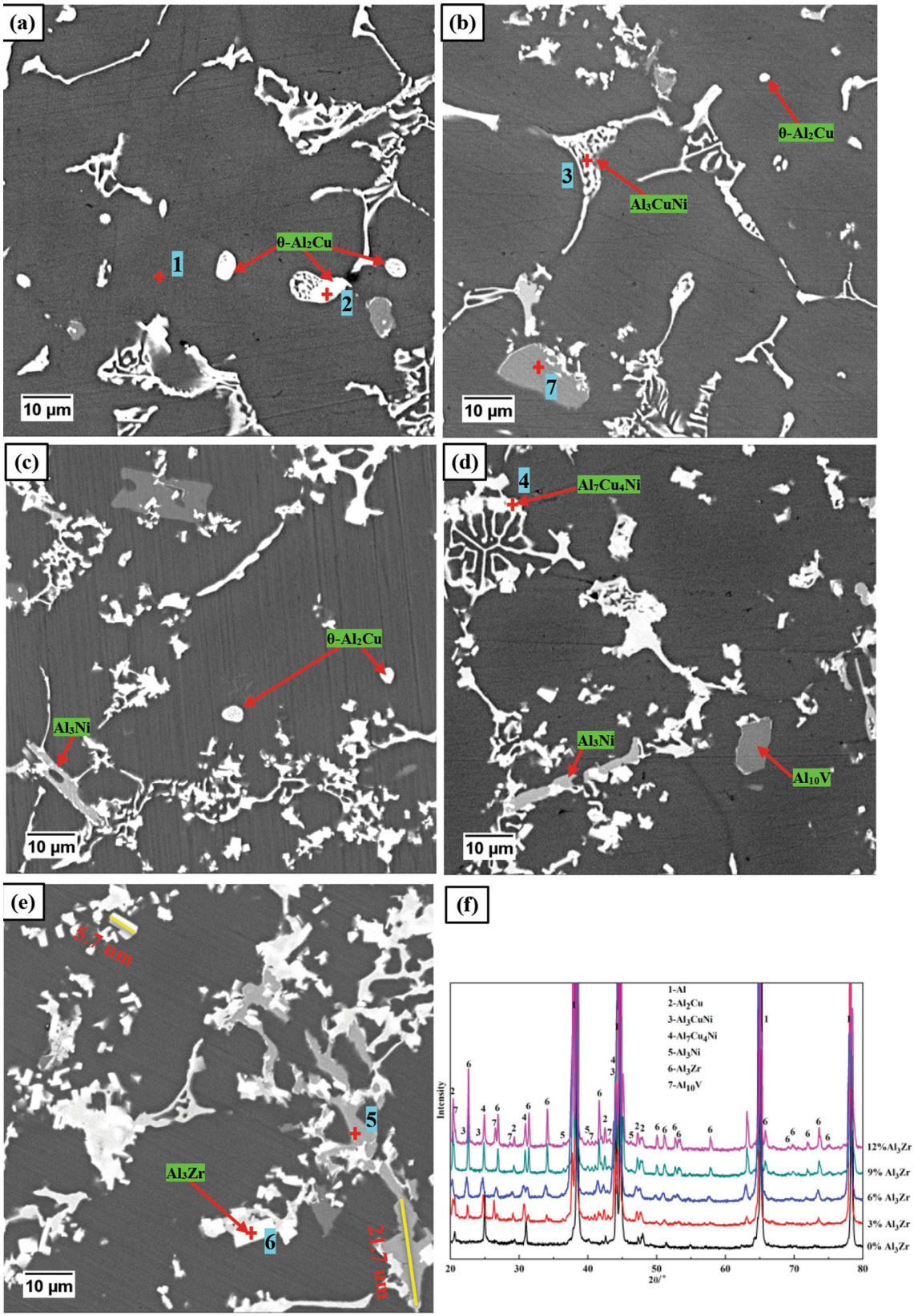

Fig. 3 Microstructure of as-cast xAl_3Zr/Al-6Cu-2Ni-0.5 V composites: (a) x = 0 wt.%, (b) x = 3 wt.%, (c) x = 6 wt.%, (d) x = 9 wt.%, and (e) x = 12 wt.% Al_3Zr. (f) XRD patterns of as-cast composites

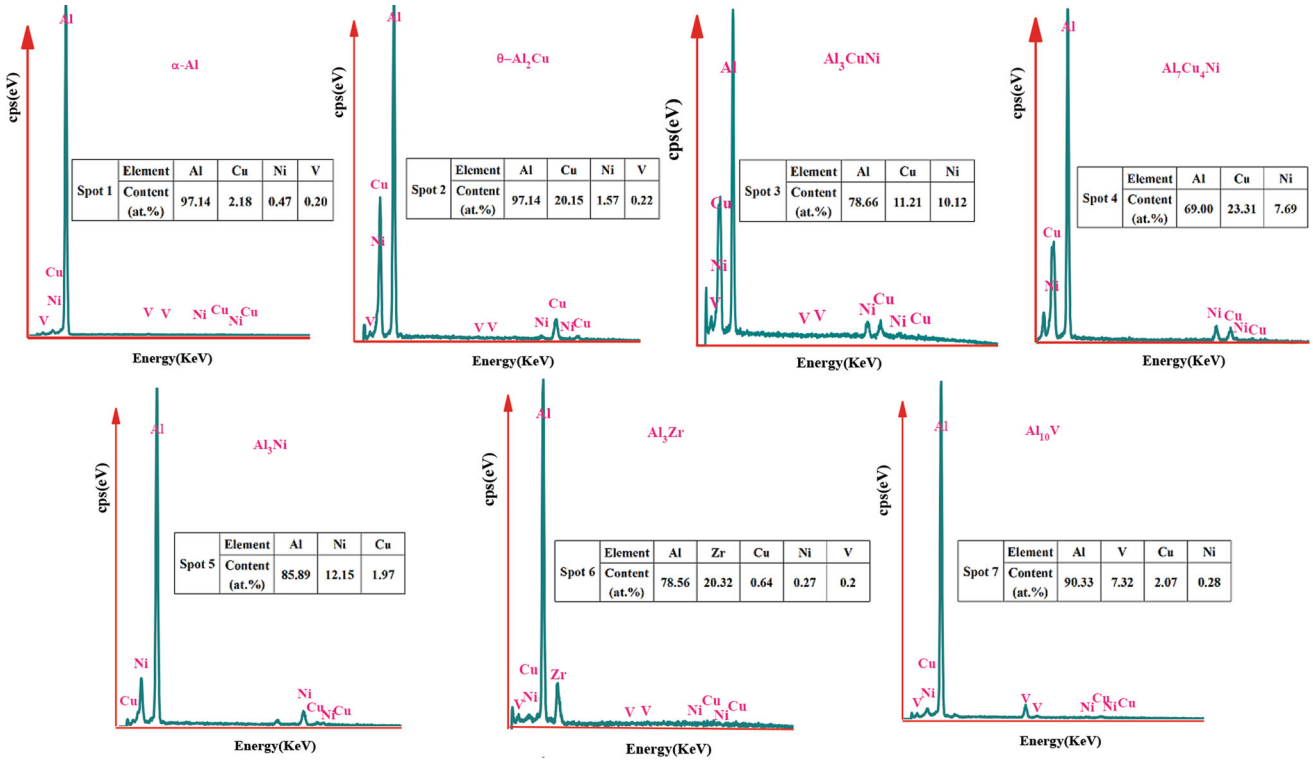

Fig. 4 EDS analysis of phases in locations shown in Fig. 3

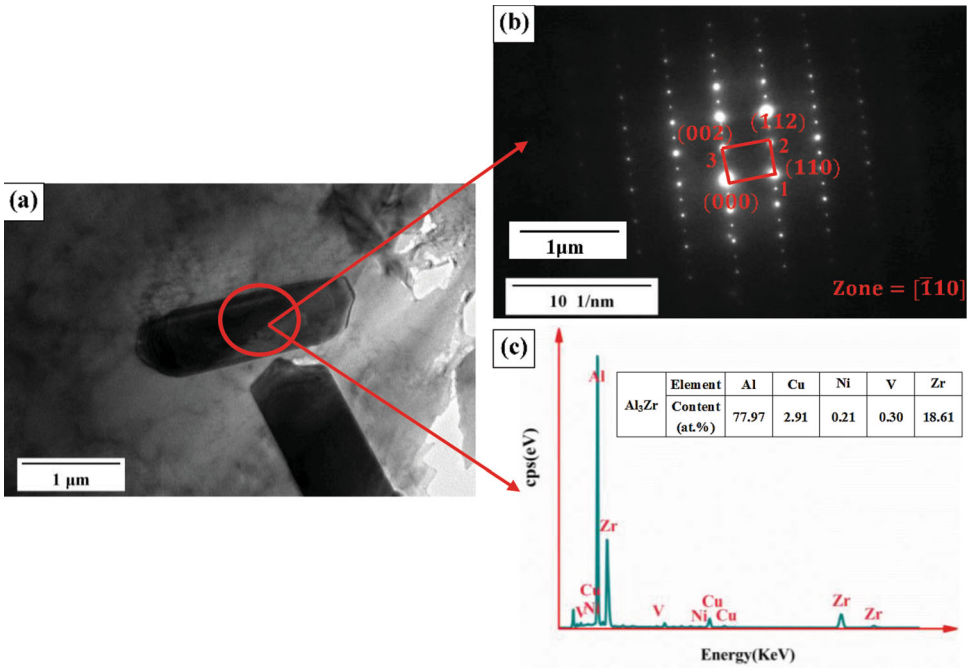

Fig. 5 TEM micrographs and SAD patterns of $D0_{23}$-Al_3Zr phase

in the range of 0-9 wt.%, but drops sharply at 12 wt.%. A similar trend is observed for the σ_{YS}; the highest σ_{YS}, 167.5 MPa, is at 6 wt.% Al_3Zr, only 10.8% higher than the base alloy. The fracture strain and elongation decrease with the increase in Al_3Zr content. These results indicate that the RT tensile properties of the as-cast composites are not improved by introducing the Al_3Zr phase. The high strength and hardness of micron-sized Al_3Zr particles can likely strengthen the matrix alloy in theory. However, the low geometric symmetry of Al_3Zr particles, coupled with the relatively stiff matrix at room temperature, easily causes cracks at the interface due to the stress concentration, which decreases the mechanical properties (Ref 15). In particular, for the composite containing 12 wt.% Al_3Zr and excessive Al_3Zr, the production of coarse Al_3Ni

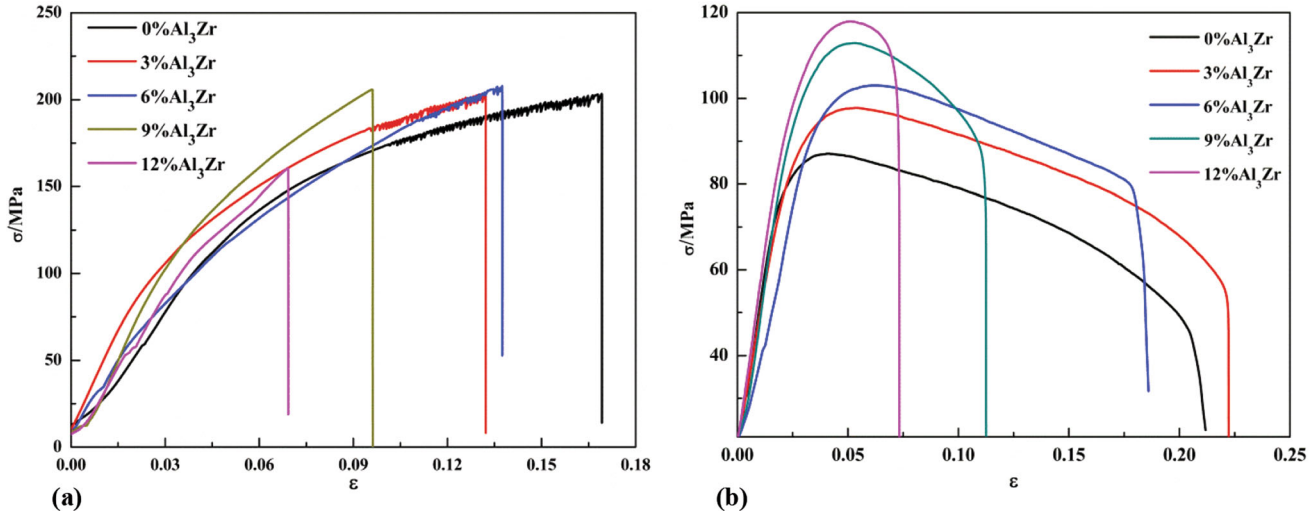

Fig. 6 Tensile stress–strain curves of as-cast xAl_3Zr/Al-6Cu-2Ni-0.5 V composites at (a) RT and (b) 350 °C

Table 2 Tensile properties of as-cast xAl_3Zr/Al-6Cu-2Ni-0.5 V composites

	σ_{UTS}, MPa		σ_{YS}, MPa		ε_F, %		Elongation, %	
Al_3Zr (wt.%)	RT	350 °C	RT	350 °C	RT	350 °C	RT	350 °C
0	203.5	87.1	151.2	76.5	16.9	21.2	6.3	14.7
3	203.8	97.8	154.2	87.7	13.2	22.2	4.6	17.9
6	207.9	103.1	167.5	95.9	13.8	18.6	4.9	11.3
9	205.9	112.9	154.7	104.8	9.6	11.3	3.8	6.7
12	160.4	118.0	129.8	109.2	6.9	7.3	2.0	2.9

phase is the likely reason for the sharp decline of mechanical properties. This composition has an elongation of only 2%. Nevertheless, the tensile properties of most of the as-cast composites reach some heat-resistant Al-alloys in services, such as M138 (180-220 MPa) and M244 (170-210 MPa) (Ref 45).

The HT tensile test results show that the σ_{UTS} and σ_{YS} of all composites significantly improved with the increasing Al_3Zr content (shown in Fig. 6b). The relationship between σ_{UTS} and σ_{YS} is approximately linear with $D0_{23}$-Al_3Zr volume fraction (f_{vol}). The relation between f_{vol} and the HT properties of the as-cast composites can be expressed as $\sigma_{UTS} = 304.7f_{vol} + 86.7$ and $\sigma_{YS} = 329f_{vol} + 76.6$, respectively. Here, the 3, 6, 9, and 12 wt.% of Al_3Zr are converted to volume fractions of 0.034, 0.062, 0.077 and 0.103, respectively. The highest tensile strength of 118 MPa occurs in the composite containing 12 wt.% Al_3Zr, 34.8% higher than the base alloy. The HT strengthening effect of the Al_3Zr phase is far more significant than at RT because the composite matrix is soft at high temperatures and has high plasticity. The soft matrix can passivate the crack's tip initiated due to the interfacial stress concentration and delay the crack propagation. Thus, the highly thermally stable Al_3Zr particles better hinder the dislocation movement (Ref 1). At 350 °C, we believe that the strength and hardness of nano-θ′-Al_2Cu particles will somewhat decrease. Therefore, Al_3Zr particles with high thermal stability provide a portion of the matrix's strength at high temperatures. Al_3Zr is a hard particle with a size greater than a few microns. Here, we do not use the Orowan mechanism to explain the strengthening mechanism but use the strengthening mechanism of particle-reinforced composites to explain. The particle reinforcement mechanism of composite materials is suitable for particle sizes larger than 1 μm of hard particles. At this point, the matrix plays a major bearing role, while the particles not only hinder the dislocation movement of the matrix, but also bear the role of load and constrain the deformation of the matrix. At this point, the yield strength of the composite material can be expressed as the following formula (Ref 46):

$$\sigma_y = \sqrt{\frac{\sqrt{3}G_m G_p b V_p^{1/2}}{\sqrt{2}d(1 - V_p)c}} \quad \text{(Eq 1)}$$

where G_m is the shear modulus of the matrix, b is the Bernoulli vector, V_p is the volume fraction of the particles, d is the average diameter of the particles, G_p is the shear modulus of the particles, c is a constant, and G_p/c is the particle strength. The smaller the particle size and the larger the volume fraction, the better the strengthening effect. Generally, in particle-reinforced composites, the particle diameter is 1 to 50 μm. The particle spacing is 1-25 μm. The volume fraction of particles is about 5-50%. Due to the large particle size, it is subjected to tensile force during the stretching process and is transferred to the matrix through the interface, making the matrix stronger.

The RT tensile fracture in Fig. 7 shows that many tetragonal Al_3Zr particles are exposed on the fracture surface, and these particles are not surrounded by dimples, indicating cleavage at the Al_3Zr-matrix interface. The matrix becomes stiff and

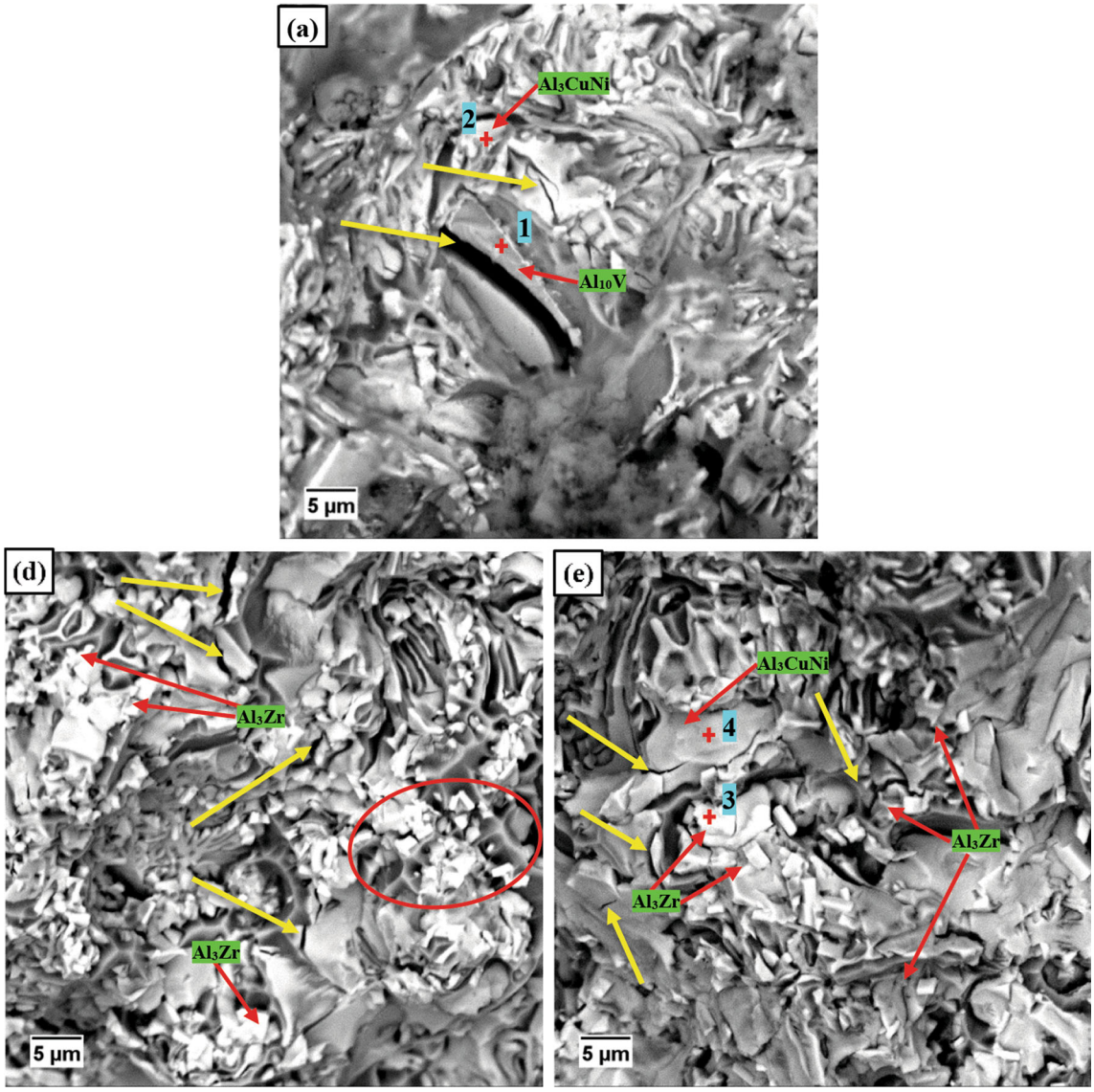

Fig. 7 RT tensile fracture morphology of as-cast xAl_3Zr/Al-6Cu-2Ni-0.5 V composites: (a) 0, (b) 9 and (c) 12 wt.%. The corresponding EDS analysis results are presented in Fig. 8

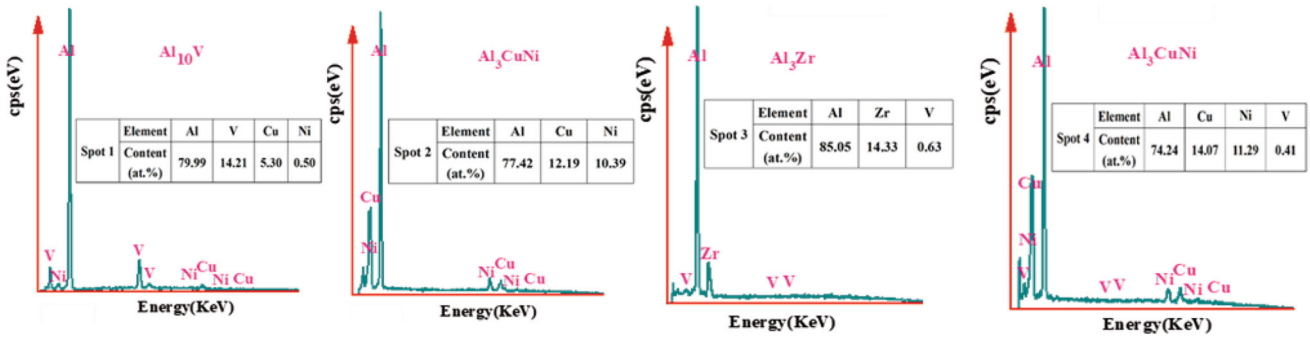

Fig. 8 EDS analysis of phases in locations shown in Fig. 7

sensitive to cracking at RT due to the dissolution of Cu, Ni, V, and Zr atoms, leading to interfacial stress concentration cracking, and the yellow arrow points to the crack. This observation is supported by the stress–strain curves presented in Fig. 7(a), where the brittle fracture is observed immediately after reaching the peak strength. In addition, some coarse Al_3CuNi and $Al_{10}V$ phases show signs of fragmentation, indicating their presence at the brittle interface, which is

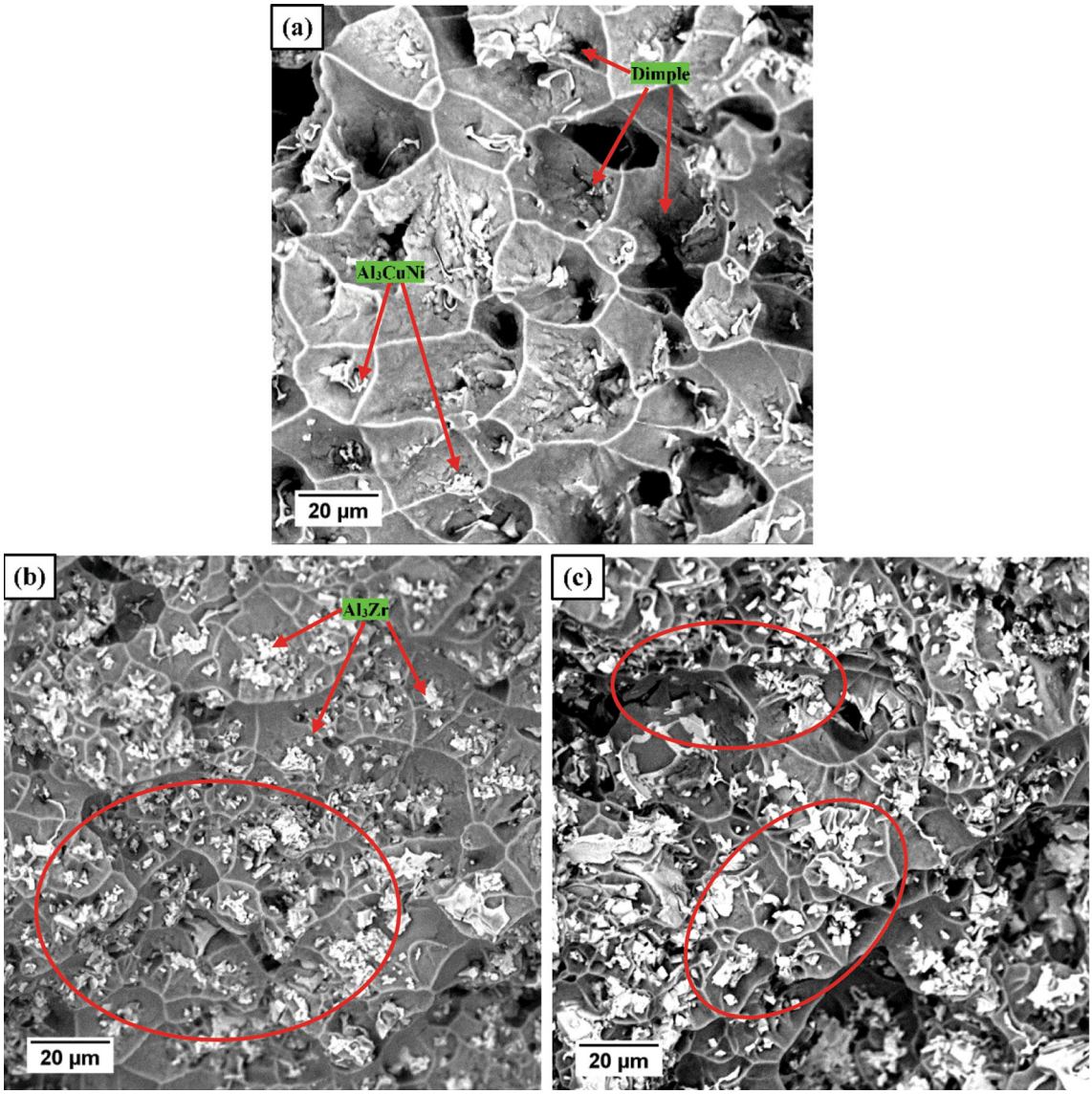

Fig. 9 HT tensile fracture of as-cast xAl_3Zr/Al-6Cu-2Ni-0.5 V composites: (a) 0, (b) 9 and (c) 12 wt.%

detrimental to the RT strength. Therefore, the cleavage fracture of the interface and the brittle fracture of Al_3CuNi and $Al_{10}V$ phases are the failure modes of the as-cast composites.

Figure 9 shows that many dimples covered the HT tensile fracture surface. It can be seen that the fracture surface of the unreinforced matrix alloy (shown in Fig. 9a) is covered with many coarse and deep dimples, indicating that large plastic deformation occurs before fracture and the dislocation slip and movement are significant. There are second-phase Al_3Zr particles at the core of most dimples in the composites. The dimples are formed by nucleation and growth of micropores at the Al_3Zr particle-matrix interface, followed by microvoid coalescence as the failure mode. With the increase in Al_3Zr content, the dimple size becomes smaller due to a reduction in interparticle spacing that inhibits the growth of each dimple and hindrance dislocation movement by the high-temperature stable Al_3Zr particles. Therefore, the HT strengthening mode of composites belongs to particle precipitation strengthening.

3.3 Microstructure of the Heat-Treated Composites

Figure 10 shows the microstructure of the composites with different Al_3Zr contents after the T6 heat treatment. Figure 10(a) and (b) are the low magnification images, and Fig. 10(c)-(g) are the high magnification images of the samples after metallographic corrosion. It can be observed from Fig. 10(b) that the edges and corners of some tetragonal Al_3Zr particles become smooth, and their shape changes to an ellipse or circle. The EDS (Fig. 11) elemental analysis shows that the atomic ratio of Al and (Zr + Ni + V + Cu) in the white oval or round particles are close to 3:1. XRD analysis (Fig. 12) shows that the T6 heat-treated specimens contain the Al_3Zr phase. TEM SAD analysis in Fig. 13(a) and (c) shows that these particles are $D0_{23}$-Al_3Zr phases with tetragonal lattice unit cells. The T6 heat treatment has not changed the crystal structure of Al_3Zr but has increased the dissolved Cu and Ni in it, as seen in Fig. 13(e), so it is more suitable to express it in the form of Al_3(Zr, Cu, Ni). Most tetragonal Al_3Zr particles retain the same size as the as-cast composite after heat treatment, indicating its thermal stability temperature is above 500 °C. It

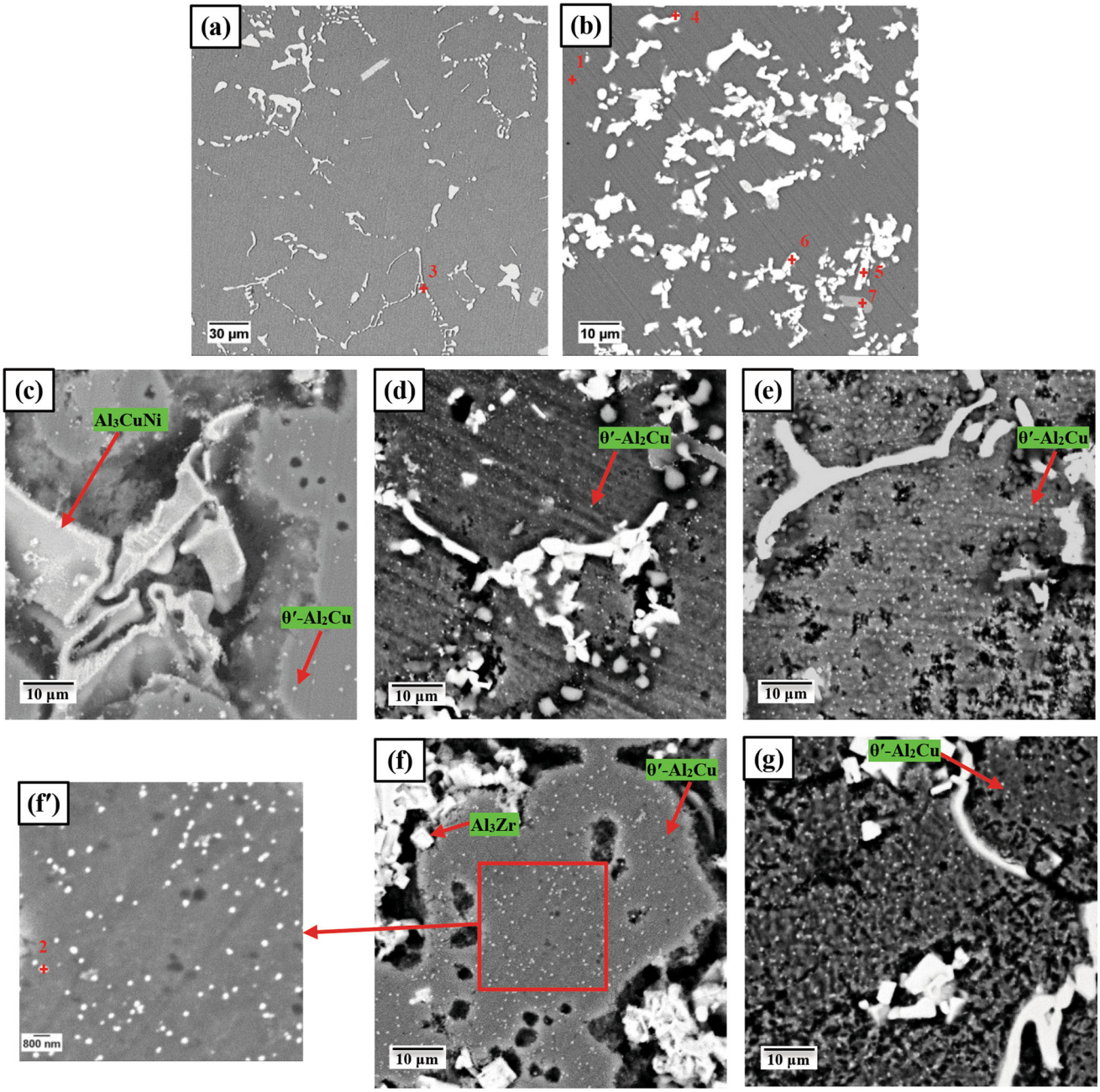

Fig. 10 Microstructure of the xAl_3Zr/Al-6Cu-2Ni-0.5 V composites after T6 heat treatment. Low magnification: (a) base alloy, (b) 9 wt.% Al_3Zr composite; High magnification: (c) base alloy, (d) 3 wt.% Al_3Zr composite, (e) 6 wt.% Al_3Zr composite, (f) 9 wt.% Al_3Zr composite, (f') partial enlargement of image f, (g) 12 wt.% Al_3Zr composite

can be observed from the high magnification images that after introducing Al_3Zr, the θ′-Al_2Cu precipitations in the composites are more than that in the matrix alloy (Fig. 10a), and the size of θ′-Al_2Cu precipitation is slightly reduced as a whole (approximately 200-300 nm). However, the morphology, quantity, and size of θ′-Al_2Cu in composites with different content of Al_3Zr are not significantly different.

Fine and dispersed particles also precipitate in the composite matrix, as visible in the high magnification images (*a*′) and (*b*′) in Fig. 10. Since there is no powder diffraction file (PDF) for the θ′-Al_2Cu phase in the Jade 6.5 database. In order to confirm that these dispersed nanoparticles are θ′-Al_2Cu, the crystal structure model of the phase was established by VESTA software (see in Fig. 14a) according to the crystal structure parameters of θ′-Al_2Cu given by Dongwon Shin et al. (Ref 47) (I-4m2 (119), $a = b = 4.0273$ Å, $c = 5.7817$ Å), and the XRD patterns of the phase were simulated (see in Fig. 14b). Figure 14(b) and (d) are the selected area electron diffraction patterns (SAED) in the direction [010] of the short rod-like nano-dispersed phase, which are consistent with the electron diffraction patterns morphology of θ′-Al_2Cu phase given by Shiwei Pan et al. (Ref 48). The crystal plane spacing was calculated by diffraction spot index 1 (200), 2 (10 $\bar{2}$) and 3 ($\bar{1}$ 0 $\bar{2}$) in Fig. 14(d) is consistent with the crystal plane spacing theoretically calculated by the lattice constant provided by Dongwon Shin et al. (Ref 47). Combined with the EDS analysis

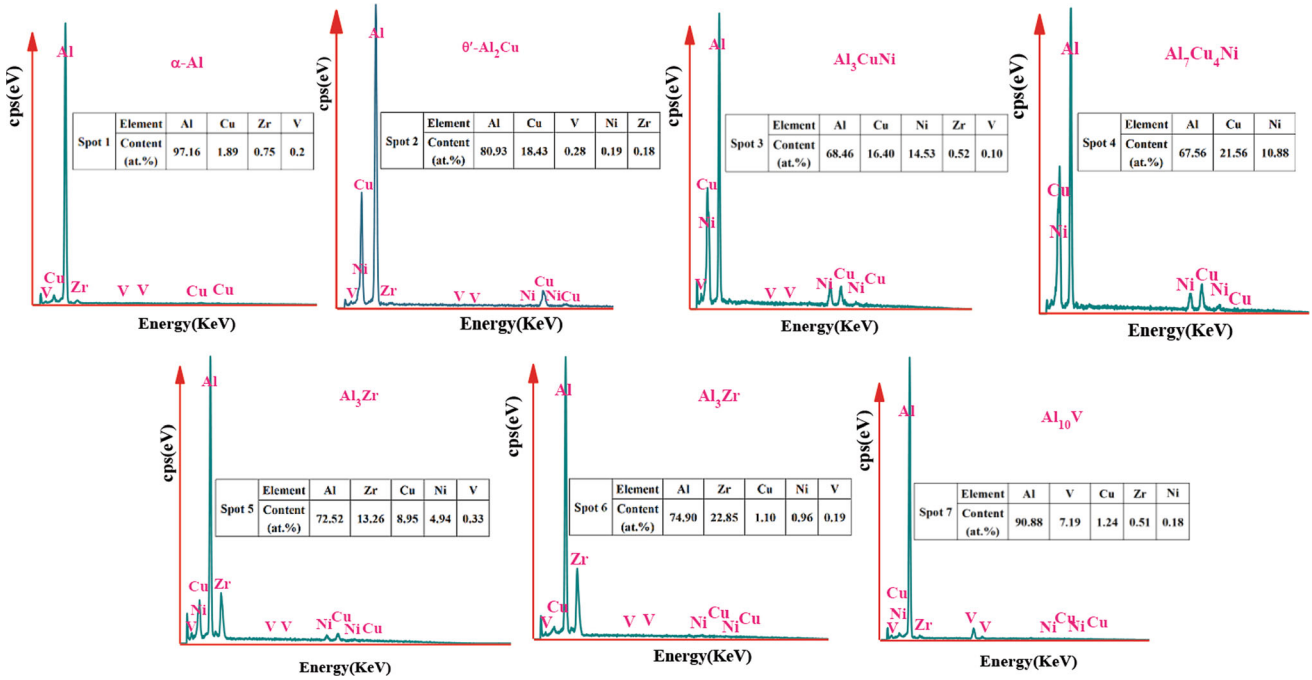

Fig. 11 EDS analysis of phases in locations shown in Fig. 10

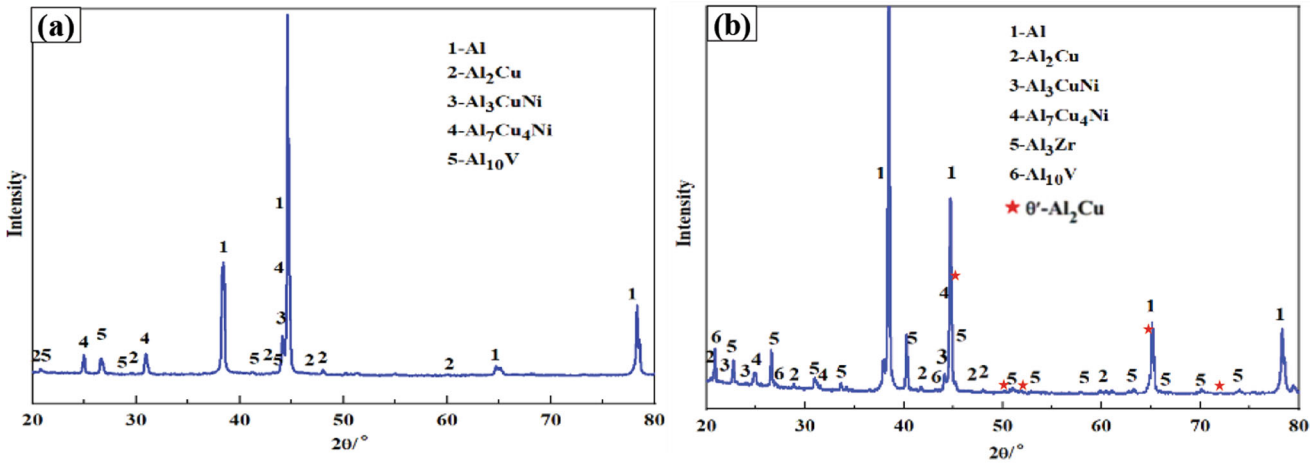

Fig. 12 XRD patterns of the base alloy (a) and composite (b) after T6 heat treatment

of the nano-dispersed particles (Fig. 11), it can be confirmed that the nano-dispersed phase is the θ′-Al_2Cu phase, and the crystal structure is tetragonal. According to the simulated diffraction pattern of θ′-Al_2Cu phase (Fig. 13b), the diffraction peak of this phase is represented as filled star in Fig. 12. Moreover, the EDS analysis in Fig. 13(f) indicates that a small amount of Zr and V are dissolved in θ′-Al_2Cu.

3.4 Tensile Properties of the Heat-Treated Base Alloy and Al_3Zr/Al-Cu-Ni-V Composites

Although the 12 wt.%Al_3Zr composite has the highest HT tensile strength, it has lower room temperature plasticity. Thus, the composite containing 9 wt%Al_3Zr after heat treatment was selected for subsequent mechanical property research. Figure 15 shows the RT and HT tensile stress–strain curves of the base alloy and the composite after T6 heat treatment. The extracted mechanical properties are presented in Table 3. The RT σ_{UTS} of the composite containing 9 wt.% Al_3Zr reached 288.5 MPa after T6 heat treatment, 13.6 MPa higher than the T6 heat-treated base alloy, and 71.4 MPa higher than the as-cast composite containing 9 wt.%Al_3Zr. The heat-treated composite's HT σ_{UTS} reached 143.1 MPa, 15.1 MPa higher than the heat-treated base alloy, 30.2 MPa higher than the as-cast composite. The results show that the Al_3Zr phase has improved both RT and HT mechanical properties.

3.5 Discussion

The Al-Cu alloy is a heat-treatable alloy, where T6 treatment can generate fine, dispersed, and coherent θ′-Al_2Cu precipitates that can provide dispersion strengthening and induce change in the morphology of the Al-Al_3CuNi eutectic phases (Ref 14). Al_3CuNi has a network structure and provides a load-bearing

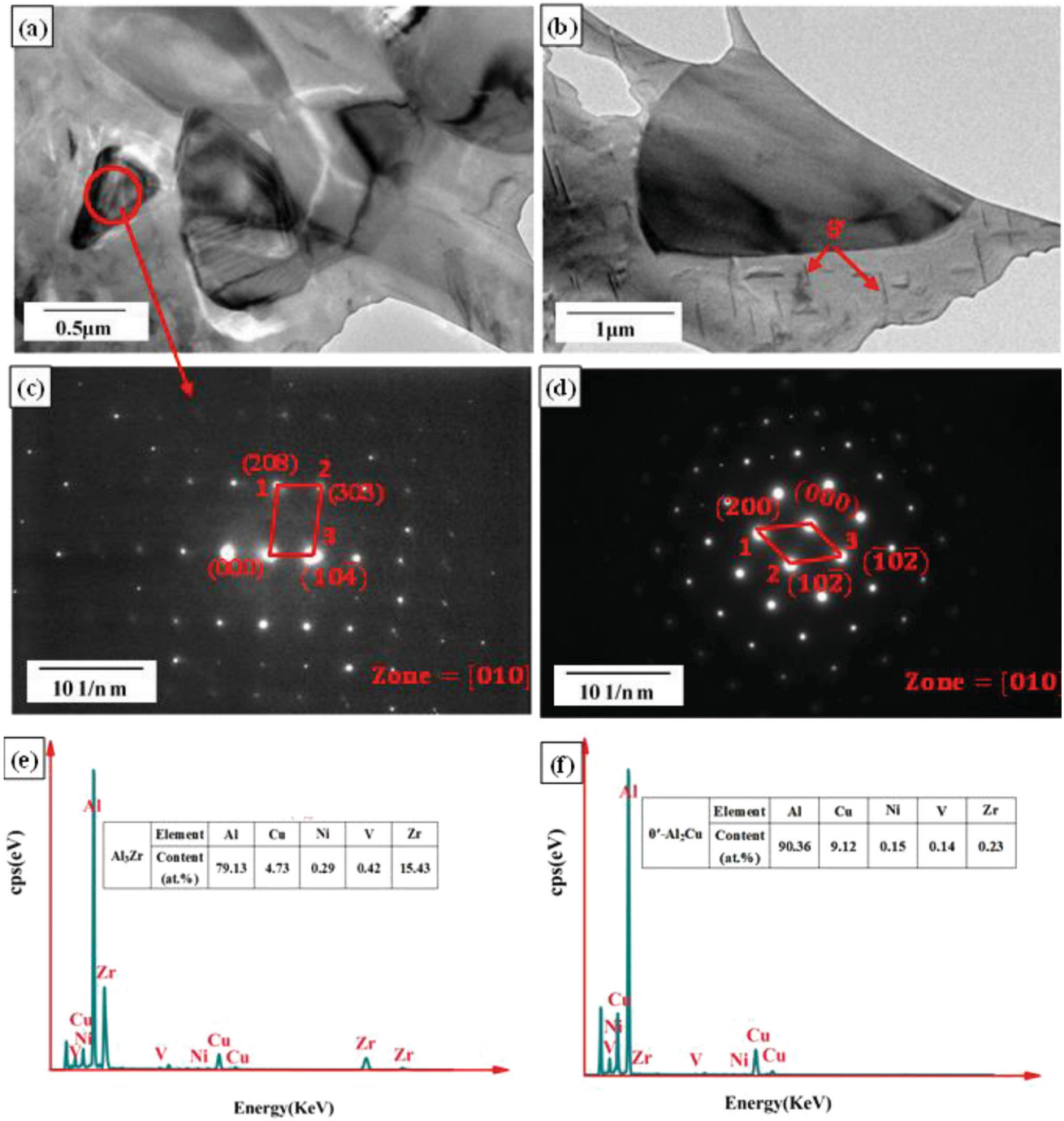

Fig. 13 TEM image and SAD patterns of $D0_{23}$-Al_3Zr and θ′-Al_2Cu: morphology of (a) $D0_{23}$-Al_3Zr an (b) θ′-Al_2Cu; SAD pattern of (c) $D0_{23}$-Al_3Zr and (d) θ′-Al_2Cu; and EDS results of (e) $D0_{23}$-Al_3Zr and (f) θ′-Al_2Cu

effect, referred to as fiber reinforcement in previous works (Ref 49, 50). This network structure is more conducive to hindering the movement of dislocations and grain boundary sliding at high temperatures. Heat treatments that break down this network lead to a reduction in mechanical properties (Ref 14, 51).

The Al_3Zr particles in the heat-treated microstructures reduce stress concentration and crack propagation rate and improve precipitation strengthening. The $D0_{23}$-Al_3Zr phase has higher thermal stability than the $L1_2$-Al_3Zr phase (Ref 38). The HT tensile fracture in Fig. 16 shows that the Al_3Zr particles are surrounded by small dimples, and these micropores dimples are not easy to generate cracks during the tensile process, thus improved the interfacial bonding strength of the matrix and resulted in improved high-temperature mechanical properties of the alloy. According to the reports, the unmodified θ′-Al_2Cu phase is stable only up to 225 °C (Ref 52, 53), which does not help provide strengthening at 350 °C. In this work, the Al_3Zr phase was introduced into the composite by adding K_2ZrF_6. The Al_3Zr phase should affect the precipitation and thermal

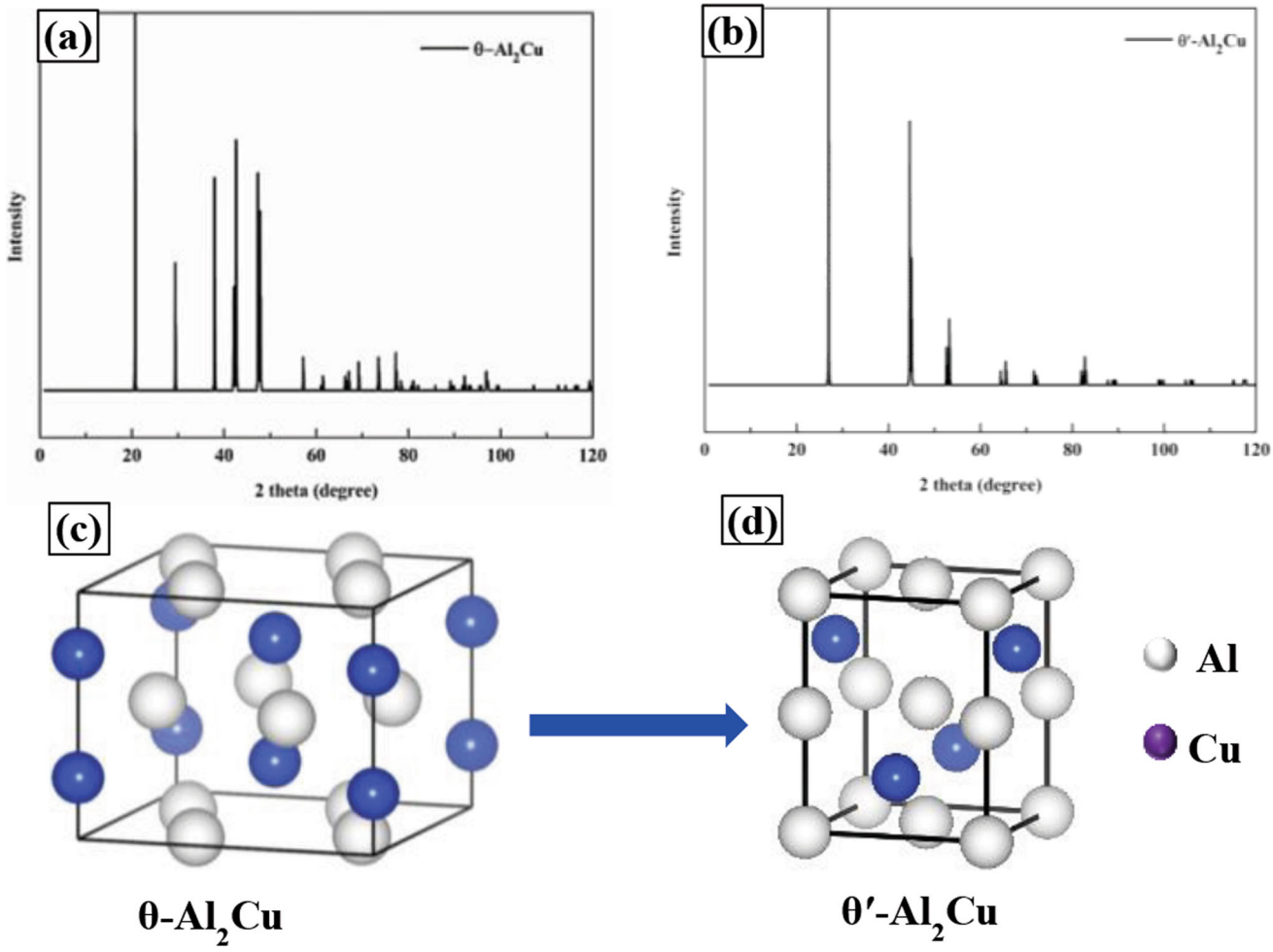

Fig. 14 Diffraction patterns and crystal structures of θ-Al_2Cu phase and θ′-Al_2Cu phase: (a) θ-Al_2Cu diffraction pattern; (b) θ′-Al_2Cu diffraction pattern; (c) θ-Al_2Cu crystal structure; (d): θ′-Al_2Cu crystal structure

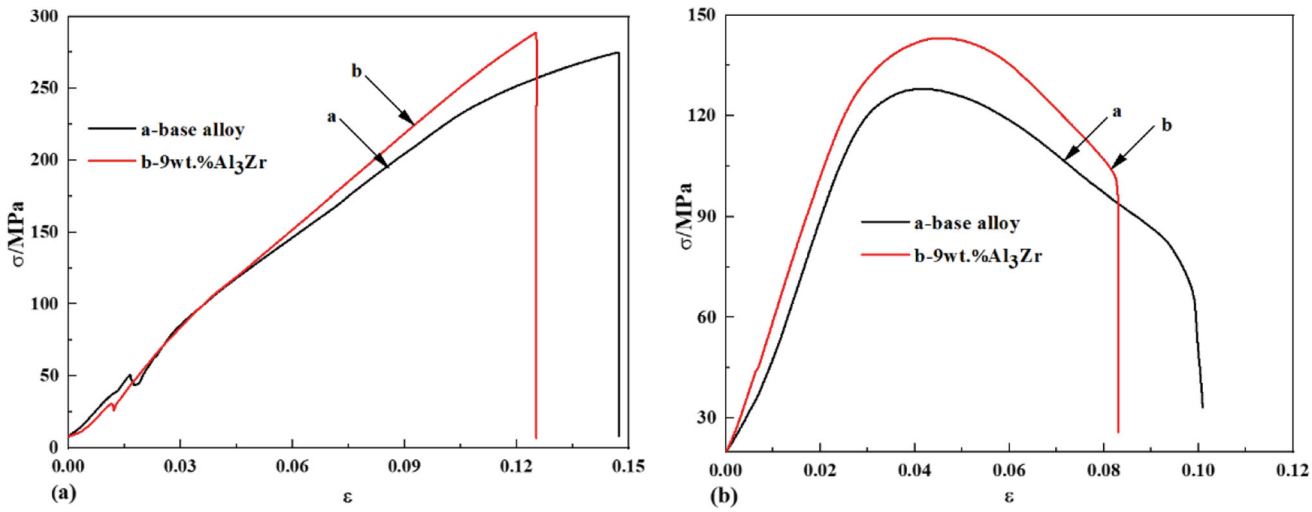

Fig. 15 RT and HT tensile stress–strain curves of the base alloy and the composite after T6 heat treatment: (a) RT; (b) HT

stability of the θ′-Al_2Cu phase. It has been reported that adding traces of Zr to Al-Cu alloy can promote precipitation and refinement of the θ′-Al_2Cu phase during the heat treatment process, improving its thermal stability (Ref 31, 33). In order to verify the effect of K_2ZrF_6 salt on the precipitation of θ′-Al_2Cu phase and its thermal stability at 350 °C, thermal exposure experiments of the composite and the base alloy after T6 heat treatment were carried out at 350 °C for 8, 16, and 24 h, and

Table 3 Tensile properties of the base alloy and the composite (9 wt.%Al_3Zr) after T6 heat treatment

	σ_{UTS}, MPa		σ_{YS}, MPa		Fracture strain, %		Elongation, %	
Material	RT	350 °C	RT	350 °C	RT	350 °C	RT	350 °C
Base alloy	274.9	128.0	240.8	123.4	14.7	10.1	5.5	4.5
Composite	288.5	143.1	250.0	136.9	12.5	8.3	4.8	3.8

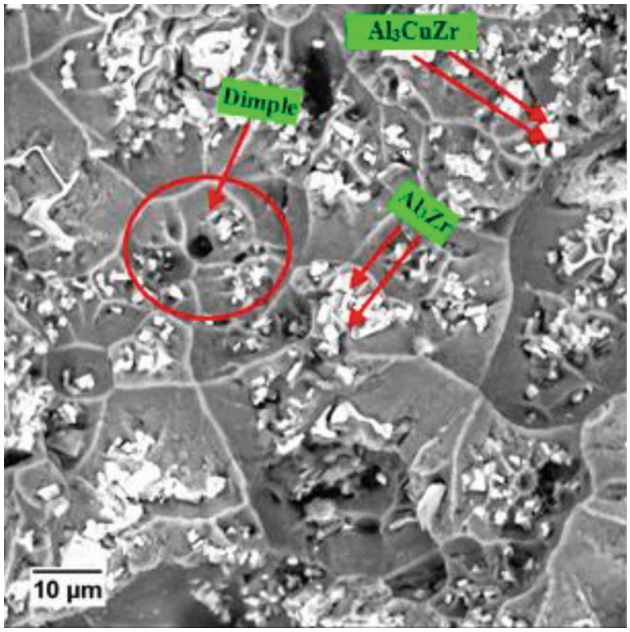

Fig. 16 HT tensile fracture of the composite after T6 heat treatment

the microstructures are shown in Fig. 17. Fig. 18 shows the EDS analysis of θ′-Al_2Cu and Al_3Zr after heat exposure for 24h. It can be seen that the size of θ′-Al_2Cu particles in the matrix after thermal exposure is smaller than that in the base alloy without adding K_2ZrF_6, indicating the addition of K_2ZrF_6 salt improves the thermal stability at 350 °C and the resistance of θ′-Al_2Cu to growth. The chemical reaction of Al melt and K_2ZrF_6 produces Al_3Zr, AlF_3, and KF (Ref 54). While AlF_3 and KF are removed by slagging, the Al_3Zr is left, which has higher solubility in the matrix above 500 °C. After quenching, only trace Zr remains in the matrix, and the Al_3Zr phase does not re-precipitate after aging because the thermal diffusion coefficient of Zr at 175 °C is very low. The EDS analysis results in Fig. 11 (spot 1) show traces of Zr in the matrix after T6 heat treatment. According to the previous studies (Ref 34, 55), Zr is mainly segregated on the θ′-Al_2Cu interface, reducing the interfacial energy and improving the thermal stability of θ′-Al_2Cu. The low thermal diffusivity of Zr and V elements can be detected in the θ′-Al_2Cu phase from the EDS analysis result in Fig. 13(f).

The addition of K_2ZrF_6 led to the precipitation of more $D0_{23}$-Al_3Zr particles, and quenching increased the density of thermal dislocations and vacancies (Ref 56-59). In the subsequent aging process, although the high dislocation density can annihilate many quenching vacancies, it inhibits the precipitation of GP zone to a certain extent. However, the existence of high dislocation density reduces the activation energy of thermal diffusion of the precipitated phase, promotes nucleation, and provides channels for diffusion, promotes the diffusion of solute, and promotes nucleation and growth (Ref 56, 59). In other words, the high dislocation density provides a preferred nucleation site for θ′ phase, which strongly depends on the nucleation of defects such as dislocation, and increases the nucleation density in the composite and reduces the size of the precipitated phase, so that the precipitated phase in the composite presents a fine and dispersive distribution.

Moreover, we believe the possible reason for the increasing precipitation amount and refining of θ′-Al_2Cu is the "traffic jam" effect formed by Zr with a low thermal diffusion coefficient in the aluminum matrix. After quenching at temperatures above 500 °C, a certain amount of Zr atoms are distributed in the aluminum matrix. During artificial aging, due to the extremely low thermal diffusion coefficient of Zr, the presence of Zr hinders the diffusion of Al and Cu atoms, resulting in more Al and Cu atoms gathering together to form clusters, known as the "traffic jam" phenomenon. When the size of Al, Cu atomic clusters reaches the critical nucleation radius of the θ′-Al_2Cu phase, the θ′-Al_2Cu grain generates. More Zr atoms in the matrix will significantly increase the nucleation rate of the θ′-Al_2Cu phase, ultimately increasing the precipitation amount and refinement size of the Al_2Cu phase.

When the particle size is less than 1 μm, the strengthening increment caused by the dislocation movement hindrance can be expressed by $\Delta\sigma_{\text{Orowan}}$, and the relation is given as (Ref 60, 61):

$$\Delta\sigma_{\text{Orowan}} = \frac{0.4MG_m b}{\pi\lambda}\frac{\ln\left(\sqrt{\left(\frac{2}{3}\right)}d_p/b\right)}{\sqrt{(1-\nu)}} \quad \text{(Eq 2)}$$

$$\lambda = \sqrt{\left(\frac{2}{3}\right)}d_p\left(\sqrt{\left(\frac{\pi}{4V_p}\right)} - 1\right) \quad \text{(Eq 3)}$$

where M is the average orientation factor ($M_{\text{Al}} = 3.06$), λ is the spacing between particles, d_P is the average particle size, b is the Burgers vector, V_P is the volume fraction of strengthened particles, G_{m} is the shear modulus of the matrix, and ν is the Poisson's ratio.

It is noted that the composite designed in this work has the highest RT tensile strength of 288.5 MPa, the yield strength of 250 MPa, and the elongation of 4.8%. The RT tensile strength is far higher than that of some German MAHLE heat-resistant Al-alloys such as M126 (180-220 MPa), M380 (180-220 MPa), and M244 (170-210 MPa). The RT tensile elongation also exceeds that of the above alloys (El ≈ 1%). The maximum HT tensile strength of the composites in this work is 143 MPa, which exceeds the HT tensile strength of many heat-resistant Al-alloys reported in recent years (shown in Table 4)

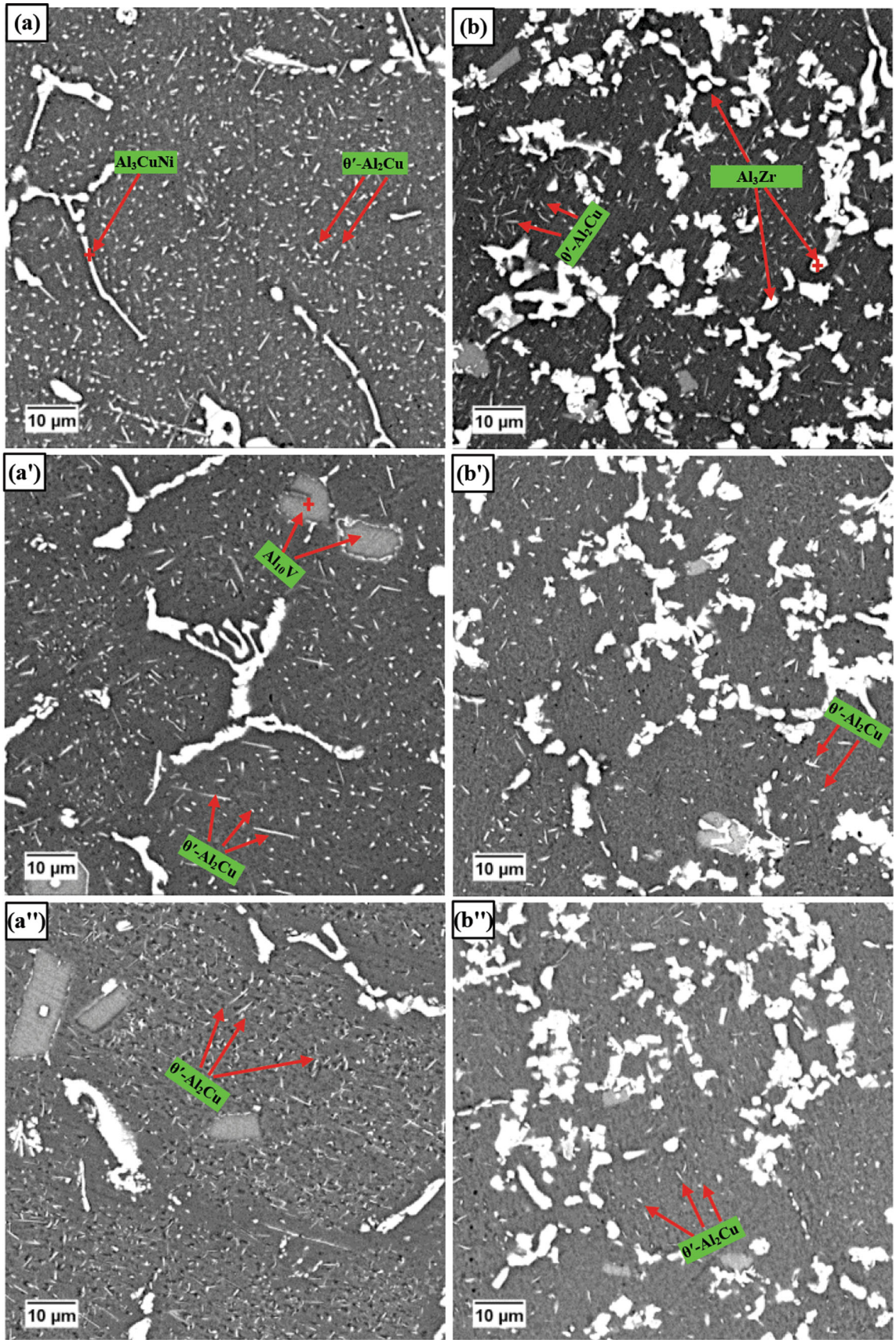

Fig. 17 Microstructure after heat exposure at 350 °C for different times (base alloy): (a) 8 h, (a′) 16 h, and (a″) 24 h; composite: (b) 8 h, (b′) 16 h, and (b″) 24 h

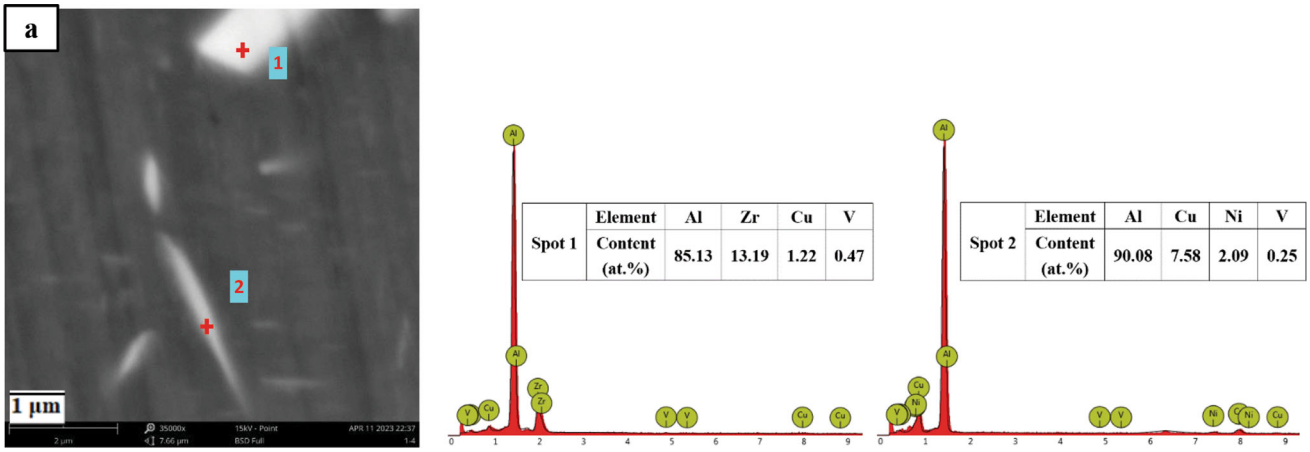

Fig. 18 EDS analysis of θ′-Al_2Cu and Al_3Zr after heat exposure for 24 h

Table 4 Comparison of tensile strength at 350 °C with other heat-resistant Al-alloys

Materials composition (wt.%)	Temperature (°C)	σ_{UTS} (MPa)	Year	References
9 wt.%Al_3Zr/Al-6Cu-2Ni-0.5 V	350	143	2021	Present work
rGO/Al	350	128	2020	Ref 62
(2% Al_3Zr + 15.2% Al_3Ni)/Al-1 Mg-0.8Mn-0.8 V	350	82	2020	Ref 15
Al-12Si-3Cu-1.5Ni	350	≈ 62	2019	Ref 17
Al-12Si-4Cu-2Ni-1 Mg-AlNp	350	106	2019	Ref 63
Al-12.95Si-3.57Cu-0.72 Mg-0.91Ni-0.53Fe-0.4Er	350	117	2019	Ref 64
Al-12Si-3.5Cu-2Mn-1Cr	350	106	2018	Ref 65
ZL109	350	67.4	2018	Ref 65
Al-(11-13) Si-(0.5-1.5) Cu-(0.8-1.3) Mg-(0.8-1.5) Ni				
Al-12.01Si-3.53Cu-0.189Fe-2.12Mn	350	83	2018	Ref 65
Al-12.21Si-3.42Cu-0.192Fe-2.02Mn-0.5Cr	350	95	2018	Ref 65
Al-11.79Si-3.33Cu-0.172Fe-2.05Mn-1Cr	350	106	2018	Ref 65
Al-11.98Si-3.38Cu-0.188Fe-2.01Mn-1.5Cr	350	91	2018	Ref 65
Al-13Si-4Cu-2Ni-1 Mg-0.25Mn	350	≈ 92	2018	Ref 66
A1-8.2AlN	350	123	2018	Ref 67
A1-0.4Cu-8.2AlN	350	119	2018	Ref 67
A1-0.4Fe-8.2AlN	350	140	2018	Ref 67
Al-12Si-0.9Cu-0.8 Mg-4Ni	350	116	2017	Ref 67
Al-12.5Si-0.84 Mg-5Cu-2Ni-0.5Fe-(0.24-0.28) Cr	350	≈92	2015	Ref 68
Al-12.75Si-2.63Cu-1.93Ni	350	78.1	2012	Ref 69
Al-12.87Si-5.45Cu-1.83Ni	350	93.5	2012	Ref 69
Al-13Si-3Cu-0.6Fe-0.6Mn	340	92	2011	Ref 70
Al-13Si-5Cu-0.6Fe-0.6Mn	340	97	2011	Ref 70
Al-13Si-1.08Cu-1.05 Mg-1Ni	350	61.63	2010	Ref 16
Al-12.8Si-3.23Cu-1.01 Mg-1Ni	350	61.71	2010	Ref 16
Al-12.57Si-1.02Cu-1.23 Mg-1.07Ni-0.04Mn	350	67.07	2008	Ref 71
Al-12.57Si-1.02Cu-1.23 Mg-1.07Ni-0.15Mn	350	75.62	2008	Ref 71
Al-12.57Si-1.02Cu-1.23 Mg-1.07Ni-0.4Mn	350	71.92	2008	Ref 71

(Ref 15-17, 62-71), indicating that the composite developed in this work has the potential to be applied above 300 °C.

4. Conclusion

xAl_3Zr/Al-6Cu-2Ni-0.5 V composites were prepared by in situ reaction of K_2ZrF_6 and Al-alloy melt. The following conclusions are drawn:

(1) The room temperature tensile strength of the as-cast xAl_3Zr/Al-6Cu-2Ni-0.5 V composites has no noticeable increase after introducing Al_3Zr particles, but the high-temperature tensile and yield strengths are significantly improved. The highest tensile strength occurs in the composite containing 12 wt.%Al_3Zr, reaching 118 MPa, 34.8% higher than the base alloy.

(2) After heat treatment, the room and high-temperature mechanical properties of the base alloy and the composite containing 9 wt.%Al_3Zr are improved. The compos-

ite's room and high-temperature tensile strengths reach the maximum levels of 288.5 and 143.1 MPa.

(3) The high-temperature strengthening mechanism of the as-cast composite is mainly the three-dimensional network of Al_3CuNi and the precipitation strengthening by the $D0_{23}$-Al_3Zr particles. After T6 heat treatment, the strengthening mechanism of the composite is mainly the dispersion strengthening of fine and dispersed θ′-Al_2Cu phase and the precipitation strengthening $D0_{23}$-Al_3Zr, and Al_3CuNi phases with high thermal stability. Adding K_2ZrF_6 into Al-Cu-Ni-V alloy melt can improve the thermal stability, refinement, and precipitation of the θ′-Al_2Cu phase.

Acknowledgments

The authors acknowledge the Special project of material processing of Guangxi Key Laboratory of Processing for Non-ferrous Metal and Featured Materials (2021GXMPSF04); Youth Fund of Guangxi Key Laboratory of Processing for Non-ferrous Metal and Featured Materials (GXYSYF1806); Special funds for local scientific and technological development under the guidance of the central government in 2021(GuiKeZY21195030); Guangxi Science and Technology Base and Talent Project in 2022 (GuiKeAD21238010).

References

1. J. Sun et al., Microstructure and Tensile Properties of a Cast Eutectic Al-Si-Cu Alloy Modified by Zr and V. Metals and Materials International, 2021: p. 1-14
2. H. Li et al., Investigation on the Asymmetric Creep Ageing Behaviour of 2195-T84 Al-Li Alloy under Different Tensile and Compressive Stress Levels, *Intermetallics*, 2021, **131**, p 107078
3. N. Bello, C. Larignon, and J. Douin, Long-Term Thermal Ageing of the 2219-T851 and the 2050-T84 Al-Cu Alloys, *Mater. Today Commun.*, 2021, **29**, p 102834
4. M. Zamani et al., The Role of Transition Metal Additions on the Ambient and Elevated Temperature Properties of Al-Si Alloys, *Mater. Sci. Eng. A*, 2017, **693**, p 42–50
5. M. Javidani and D. Larouche, Application of Cast Al-Si Alloys in Internal Combustion Engine Components, *Int. Mater. Rev.*, 1989, **59**(3), p 132–158
6. L. Zuo et al., Microstructure, Tensile Properties and Creep Behavior of Al-12Si-35Cu-2Ni-0.8Mg Alloy Produced by Different Casting Technologies, *J. Mater. Sci. Technol.*, 2018, **34**(7), p 1222–1228
7. J.L. Cann et al., Sustainability Through Alloy Design: Challenges and Opportunities. Progress in Materials Science, 2020: p. 100722
8. K.E. Knipling, D.C. Dunand, and D.N. Seidman, Criteria for Developing Castable, Creep-Resistant Aluminum-Based Alloys: A Review, *Z. Met.*, 2006, **97**(3), p 246–265
9. K.E. Knipling, D.C. Dunand, and D.N. Seidman, Nucleation and Precipitation Strengthening in Dilute Al-Ti and Al-Zr Alloys, *Metall. Mater. Trans. A.*, 2007, **38**(10), p 2552–2563
10. K.E. Knipling, D.C. Dunand, and D.N. Seidman, Atom Probe Tomographic Studies of Precipitation in Al-0.1 Zr-0.1 Ti (at.%) Alloys, *Microsc. Microanal.*, 2007, **13**(6), p 503
11. S. Pogatscher et al., Process-Controlled Suppression of Natural Aging in an Al-Mg-Si Alloy, *Scr. Mater.*, 2014, **89**, p 53–56
12. R.K. Marceau et al., Solute Clustering in Al-Cu-Mg Alloys during the Early Stages of Elevated Temperature Ageing, *Acta Mater.*, 2010, **58**(15), p 4923–4939
13. B. Chen et al., Effect of Solution Treatment on Precipitation Behaviors and Age Hardening Response of Al-Cu Alloys with Sc Addition, *Mater. Sci. Eng. A*, 2011, **530**, p 607–617
14. J. Chen et al., Contributions to High Temperature Strengthening from Three Types of Heat-Resistant Phases Formed during Solidification, Solution Treatment and Ageing Treatment of Al-Cu-Mn-Ni Alloys Respectively, *Mater. Sci. Eng. A*, 2020, **772**, p 138819
15. L. Pan et al., High-Temperature Mechanical Properties of Aluminum Alloy Matrix Composites Reinforced with Zr and Ni Trialumnides Synthesized by In Situ Reaction, *Metall. Mater. Trans. A*, 2020, **51**(1), p 214–225
16. Y. Li et al., Quantitative Comparison of Three Ni-Containing Phases to the Elevated-Temperature Properties of Al-Si Piston Alloys, *Mater. Sci. Eng. A*, 2010, **527**(26), p 7132–7137
17. L. Zuo et al., Effect of δ-Al3CuNi Phase and Thermal Exposure on Microstructure and Mechanical Properties of Al-Si-Cu-Ni Alloys, *J. Alloy. Compd.*, 2019, **791**, p 1015–1024
18. W. Kasprzak, B.S. Amirkhiz, and M. Niewczas, Structure and Properties of Cast Al-Si Based Alloy with Zr-V-Ti Additions and its Evaluation of High Temperature Performance, *J. Alloy. Compd.*, 2014, **595**, p 67–79
19. A.V. Rodrigues et al., Microstructure and Tensile/Corrosion Properties Relationships of Directionally Solidified Al-Cu-Ni Alloys, *Met. Mater. Int.*, 2018, **24**(5), p 1058–1076
20. S. Gencalp Irizalp, N. Saklakoglu, and B.S. Yilbas, Characterization of Microplastic Deformation Produced in 6061-T6 by using Laser Shock Processing, *Int. J. Adv. Manuf. Technol.*, 2014, **71**(1), p 109–115
21. M.G.C. Xavier et al., Effects of Ni and Co on the Corrosion Resistance of Al-Si-Cu-Zn-Fe Alloys in NaCl Solution, *Metals*, 2022, **12**(4), p 645
22. S. Toschi, Optimization of A354 Al-Si-Cu-Mg Alloy Heat Treatment: Effect on Microstructure, Hardness, and Tensile Properties of Peak Aged and Overaged Alloy, *Metals*, 2018, **8**(11), p 961
23. A. Bjurenstedt, S. Seifeddine, and A. Jarfors, The Effects of Fe-Particles on the Tensile Properties of Al-Si-Cu Alloys, *Metals*, 2016, **6**(12), p 314–314
24. H. Huang et al., Microstructure Characteristics and Elevated-Temperature Tensile Properties of Al-7Si-0.3 Mg Alloys with Zr and Hf Addition, *J. Mater. Eng. Perform.*, 2021, **30**(12), p 9059–9066
25. K.E. Knipling, D.C. Dunand, and D.N. Seidman, Precipitation Evolution in Al-Zr and Al-Zr-Ti Alloys during Isothermal Aging at 375-425°C, *Acta Mater.*, 2008, **56**(1), p 114–127
26. Fan et al., The Effect of Introducing the Al-Ni Eutectic Composition into Al-Zr-V Alloys on Microstructure and Tensile Properties, *Mater. Sci. Eng. A Struct. Mater. Prop. Misrostruct. Process.*, 2016, **654**, p 228–235
27. M. Zedalis and M. Fine, Lattice Parameter Variation of Al3 (Ti, V, Zr, Hf) in Al-2 AT.%(Ti, V, Zr, Hf) Alloys, *Scr. Metall.*, 1983, **17**(10), p 1247–1251
28. S.K. Shaha et al., Thermal Stability of (AlSi) x (ZrVTi) Intermetallic Phases in the Al-Si-Cu-Mg Cast Alloy With Additions of Ti, V, and Zr, *Thermochim. Acta*, 2014, **595**, p 11–16
29. D. Erdeniz et al., Effect of Vanadium Micro-Alloying on the Microstructural Evolution and Creep Behavior of Al-Er-Sc-Zr-Si Alloys, *Acta Mater.*, 2017, **124**, p 501–512
30. Y. Fan and M.M. Makhlouf, The Effect of Introducing the Al-Ni Eutectic Composition into Al-Zr-V Alloys on Microstructure and Tensile Properties, *Mater. Sci. Eng., A*, 2016, **654**, p 228–235
31. J. Ding et al., Effect of Mo, Zr, and Y on the High-Temperature Properties of Al-Cu-Mn Alloy, *J. Mater. Res.*, 2019, **34**(22), p 3853–3861
32. K. Knipling, Precipitation evolution in Al-Zr and Al-Zr-Ti alloys during aging at 450-600°C, *Acta Mater.*, 2008, **56**(6), p 1182–1195
33. S. Mondol et al., Enhancement of High Temperature Strength of 2219 Alloys Through Small Additions of Nb and Zr and a Novel Heat Treatment, *Metall. Mater. Trans. A*, 2018, **49**(7), p 3047–3057
34. L. Jiang et al., Coupled Segregation Mechanisms of Sc, Zr and Mn at θ′ Interfaces Enhances the Strength and Thermal Stability of Al-Cu Alloys, *Acta Mater.*, 2021, **206**, p 116634
35. D. Shin et al., Solute Segregation at the Al/θ′-Al2Cu Interface in Al-Cu Alloys, *Acta Mater.*, 2017, **141**, p 327–340
36. K. Ling et al., Effect of V Additions on the Microstructure and Mechanical Properties of Al-Cu-Mg-Ag alloy. Mater. Today Commun., 2022. **33**
37. F. Zupanič et al., Quasicrystalline and L12 Precipitates in a Microalloyed Al-Mn-Cu Alloy. Mater. Today Commun., 2020. **22**

38. S. Srinivasan, P. Desch, R. Schwarz, Metastable phases in the Al3X (X= Ti, Zr, and Hf) intermetallic system. Scr. Metall. et materialia, 1991. **25**
39. H.M. Lee, J. Lee, and Z.-H. Lee, Lattice Misfit Variation of Al 3 (Ti, V, Zr) in Al-Ti-V-Zr Alloys, *Scr. Metall.*, 1991, **25**(1), p 517–520
40. T. Gao et al., Morphological Evolution of ZrAlSi Phase and its Impact on the Elevated-Temperature Properties of Al-Si Piston Alloy, *J. Alloy. Compd.*, 2013, **567**, p 82–88
41. X. Kai et al., High Strength and High Creep Resistant ZrB2/Al Nanocomposites Fabricated by Ultrasonic-Chemical In-Situ Reaction, *J. Mater. Sci. Technol.*, 2019, **35**(9), p 2107–2114
42. H. Liao, G. Li, and Q. Liu, Ni-Rich Phases in Al-12% Si-4% Cu-1.2% Mn-x% Ni Heat-Resistant Alloys and Effect of Ni-Alloying on Tensile Mechanical Properties, *J. Mater. Eng. Perform.*, 2019, **28**(9), p 5398–5408
43. B. Lin et al., Developing High Performance Mechanical Properties at Elevated Temperature In Squeeze cast Al-Cu-Mn-Fe-Ni Alloys, *Mater. Charact.*, 2019, **150**, p 128–137
44. P.B. Desch et al., Formation of Metastable L12 Phases in Al3Zr and Al-12.5%X-25%Zr (X ≡ Li, Cr, Fe, Ni, Cu), *J. Less Common Metals*, 1991, **168**, p 69
45. M. GmbH, Pistons and engine testing. 2016
46. C.Z. Xiaoming Feng, *Composite Materials*, Chongqing University Publisher, Chongqing, 2007
47. D. Shin et al., Lattice Mismatch Modeling of Aluminum Alloys, *Comput. Mater. Sci.*, 2017, **138**, p 149–159
48. S. Pan et al., Micro-Alloying Effect of Er and Zr on Microstructural Evolution and Yield Strength of Al-3Cu (wt.%) Binary Alloys, *Mater. Sci. Eng. A*, 2020, **790**, p 139391
49. L. Zuo et al., Effect of ε-Al3Ni Phase on Mechanical Properties of Al-Si-Cu-Mg-Ni Alloys at Elevated Temperature, *Mater. Sci. Eng. A*, 2020, **772**, p 138794
50. K. Bugelnig et al., Influence of 3D Connectivity of Rigid Phases on Damage Evolution during Tensile Deformation of an AlSi12Cu4Ni2 Piston Alloy, *Mater. Sci. Eng. A*, 2018, **709**, p 193–202
51. H. Zhang, Y. Liu, and T. Fan, Three-Dimensional Network Structure and Mechanical Properties of Al-Cu-Ni-Fe Cast Alloys with Gd Micro-addition, *Metall. and Mater. Trans. A*, 2021, **52**(6), p 2613–2629
52. Y. Gao et al., Stabilizing Nanoprecipitates in Al-Cu Alloys for Creep Resistance at 300° C, *Mater. Res. Lett.*, 2019, **7**(1), p 18–25
53. D. Mitlin, V. Radmilovic, and J.W. Morris, Catalyzed Precipitation in Al-Cu-Si, *Metall. Mater. Trans. Phys. Metall. Mater. Sci.*, 2000, **31**(11), p 2697–2711
54. G. Gautam et al., Strengthening Mechanisms of (Al3Zrmp + ZrB2np)/AA5052 Hybrid Composites, *J. Compos. Mater.*, 2016, **50**(29), p 4123–4133
55. A. Shyam et al., Elevated Temperature Microstructural Stability in Cast AlCuMnZr Alloys through Solute Segregation, *Mater. Sci. Eng. A*, 2019, **765**, p 138279
56. S. Dong et al., Age-Hardening Behavior of a SiCw/Al-Li-Cu-Mg-Zr Composite, *Mater. Sci. Eng. A*, 2002, **327**(2), p 213–223
57. T. Hong et al., Effects of TiB2 Particles on Aging Behavior of in-Situ TiB2/Al-Cu-Mg Composites, *Mater. Sci. Eng. A*, 2015, **624**, p 110–117
58. T. Das, P. Munroe, and S. Bandyopadhyay, The Effect of Al_2O_3 Particulates on the Precipitation Behaviour of 6061 Aluminium-Matrix Composites, *J. Mater. Sci.*, 1996, **31**(20), p 5351–5361
59. I. Dutta, S. Allen, and J. Hafley, Effect of Reinforcement on the Aging Response of Cast 6061 Al-Al 2 O 3 Particulate Composites, *Metall. Trans. A*, 1991, **22**(11), p 2553–2563
60. M. Wang et al., Mechanical Properties of in-situ TiB2/A356 Composites, *Mater. Sci. Eng. A*, 2014, **590**, p 246–254
61. A. Sanaty-Zadeh, Comparison Between Current Models for the Strength of Particulate-Reinforced Metal Matrix Nanocomposites with Emphasis on Consideration of Hall-Petch Effect, *Mater. Sci. Eng. A-Struct.*, 2012, **531**, p 112–118
62. Y.N. Zan et al., Introducing Graphene (Reduced Graphene Oxide) into Al Matrix Composites for Enhanced High-Temperature Strength, *Compos. B Eng.*, 2020, **195**, p 108095
63. K. Hu et al., A Novel Heat-Resistant Al-Si-Cu-Ni-Mg Base Material Synergistically Strengthened by Ni-Rich Intermetallics and Nano-AlNp Microskeletons, *J. Mater. Sci. Technol.*, 2019, **35**(3), p 306–312
64. S. Chankitmunkong et al., Microstructure and Elevated Temperature Mechanical Properties of a Direct-Chill Cast AA4032 Alloy with Copper and Erbium Additions, *J. Alloy. Compd.*, 2019, **782**, p 865–874
65. G. Li et al., Cr-Induced Morphology Change of Primary Mn-Rich Phase in Al-Si-Cu-Mn Heat Resistant Aluminum Alloys and its Contribution to High Temperature Strength, *Mater. Sci. Eng. A*, 2018, **709**, p 90–96
66. L. Tian et al., Elevated Re-aging of a Piston Aluminium Alloy and Effect on the microstructure and mechanical properties, *Mater. Sci. Eng. A*, 2018, **738**, p 375–379
67. X. Ma et al., Influence Mechanisms of Cu or Fe on the Microstructures and Tensile Properties at 350 °C of Network AlNp Reinforced Al Composites, *J. Alloy. Compd.*, 2018, **740**, p 452–460
68. Y. Yang et al., Effect of Cr Content and Heat-Treatment on the High Temperature Strength of Eutectic Al-Si Alloys, *J. Alloy. Compd.*, 2015, **647**, p 63–69
69. Y. Yang et al., Evolution of Nickel-Rich Phases in Al-Si-Cu-Ni-Mg Piston Alloys with Different Cu Additions, *Mater. Des.*, 2012, **33**, p 220–225
70. E.R. Wang, X.D. Hui, and G.L. Chen, Eutectic Al-Si-Cu-Fe-Mn Alloys with Enhanced Mechanical Properties at Room and Elevated Temperature, *Mater. Des.*, 2011, **32**(8–9), p 4333–4340
71. Z. Qian et al., Effects of Trace Mn Addition on the Elevated Temperature Tensile Strength and Microstructure of a Low-Iron Al-Si Piston Alloy, *Mater. Lett.*, 2008, **62**(14), p 2146–2149